

# Tension-compression asymmetry in amorphous silicon

Yuecun Wang<sup>1\*</sup>, Jun Ding<sup>2\*</sup>, Zhao Fan<sup>3\*</sup>, Lin Tian<sup>4\*</sup>, Meng Li<sup>1</sup>, Huanhuan Lu<sup>1</sup>, Yongqiang Zhang<sup>1</sup>, En Ma<sup>2†</sup>, Ju Li<sup>5†</sup>, Zhiwei Shan<sup>1†</sup>

<sup>1</sup>*Center for Advancing Materials Performance from the Nanoscale (CAMP-Nano) & Hysitron Applied Research Center in China (HARCC), State Key Laboratory for Mechanical Behavior of Materials, Xi'an Jiaotong University, Xi'an 710049, China*

<sup>2</sup>*Center for Alloy Innovation and Design (CAID), State Key Laboratory for Mechanical Behavior of Materials, Xi'an Jiaotong University, Xi'an 710049, China*

<sup>3</sup>*Department of Materials Science and Engineering, Johns Hopkins University, Baltimore, Maryland 21218, USA*

<sup>4</sup>*Institute of Materials Physics, University of Göttingen, Niedersachsen 37077, Germany*

<sup>5</sup>*Department of Nuclear Science and Engineering, and Department of Materials Science and Engineering, Massachusetts Institute of Technology, Cambridge, Massachusetts 02139, USA.*

\*These authors contributed equally to this work

†Corresponding authors e-mail: [zwshan@xjtu.edu.cn](mailto:zwshan@xjtu.edu.cn); [liju@mit.edu](mailto:liju@mit.edu); [maen@xjtu.edu.cn](mailto:maen@xjtu.edu.cn)

## Abstract

Hard and brittle materials usually exhibit a much lower strength when loaded in tension than in compression. However, this common-sense behaviour may not be intrinsic to these materials, but arises from their higher flaw sensitivity to tensile loading. Here we demonstrate a reversed and unusually pronounced tension-compression asymmetry - tensile strength exceeds compressive strength by a large margin - in submicron-sized samples of isotropic amorphous silicon. The abnormal asymmetry in the yield strength and anelasticity originates from the reduction in shear modulus and the densification of the shear-activated configuration under compression, altering the magnitude of the activation energy barrier for the elementary shear event in amorphous Si. *In-situ* coupled electrical tests corroborate that compressive strains indeed cause increased atomic coordination (metallization) by transforming some local structures from  $sp^3$ -bonded semiconducting motifs to more metallic-like sites, lending credence to the mechanism we propose. This finding opens an unexplored regime of intrinsic tension-compression asymmetry in materials.

## Introduction

Inorganic materials with covalent or ionic bonding are well known to be much stronger in compression than in tension. That is, for a given material, the experimentally recorded compressive strength ( $\sigma_c$ ) is usually much higher than the tensile strength ( $\sigma_t$ )<sup>1-3</sup>. However, this apparent tension-compression (T-C) asymmetry is not the intrinsic inelastic response of these materials, but instead originates from the very different sensitivity to pre-existing flaws (such as the internal voids, pores, and surface blemishes)<sup>4,5</sup>, under tension versus compression. Specifically, a tensile load tends to open up the flaw into an incipient crack and accelerate the crack propagation, such that fracture sets in prematurely at relatively low stresses to pre-empt global yielding<sup>6</sup>. In contrast, flaws tend to close up under a compressive load, such that the compressive yield strength is much higher and close to the intrinsic strength of the material<sup>3</sup>. A fundamental question then naturally arises, as to whether a T-C asymmetry remains when the effects of flaws are eliminated, and if it does, would  $\sigma_c$  be higher or lower than  $\sigma_t$ , by how much and why.

To answer the question posed above, we resort to samples that are initially nearly free of extended defects<sup>7</sup>, such that the chances for premature fracture are minimized<sup>8,9</sup>. One known way to this end is to reduce the physical dimensions of the tested volume, as ultrahigh strength close to the theoretical limit has been demonstrated before in micro- and nano-scale samples<sup>8,10</sup>. We, therefore, carried out quantitative compression versus tension testing of submicron-sized amorphous Si (a-Si), feasible using a nanomechanical testing system inside a transition electron microscope (TEM). Here the choice of a-Si is made, in lieu of crystalline compounds, to avoid complications due to variable slip systems, crystal anisotropy and chemical composition, not to mention a-Si is one of the most important semiconductors and a classic model material for the fundamental research of disordered matter<sup>11-15</sup>. In the following, we will demonstrate an unusual T-C asymmetry: the  $\sigma_c >> \sigma_t$  norm is reversed, and astonishingly  $\sigma_t$  exceeds  $\sigma_c$  by a large margin. This surprising observation is also corroborated in atomistic simulations.

## Results

### Tension-compression (T-C) asymmetry in submicron-sized a-Si

Submicron-sized a-Si samples, micromachined from deposited a-Si film ([Supplementary Fig. 1](#)) using focused ion beam (FIB), were tested in both tension and compression. One type of our tests used the same specimen for tension and compression, thus excluding possible artifacts from comparing different samples. This type of tension-compression (TC) sample is shown in Fig. 1a. The TC sample was first subjected to tensile loading. The gauge section elongated with increased loading, and then fractured abruptly (Fig. 1a). After the tensile fracture, the lower half of the TC sample remained intact, with its flat fracture surface perpendicular to the loading direction (Fig. 1b). This part of the sample was then used for compression, loaded under a flat diamond punch. In compression, the sample showed continuous shape change with homogeneous plastic flow after yielding. See [Supplementary Video](#) for the real-time tensile and compressive deformation processes. The corresponding engineering stress-strain curve is presented in Fig. 1c (effective size  $d = 145$  nm). The flow stress at a 5% plastic strain,  $\sim 4.5$  GPa for this sample, is taken as the yield strength in compression. In tension, however, a-Si did not yield at stresses exceeding  $\sim 4.5$  GPa, until the fracture set in at  $\sim 6.5$  GPa. It is uncertain if this fracture is preceded by yielding, with large but highly localized plastic strains that have immediately instigated failure. Another possibility is that the sudden fracture may be triggered prematurely by minor flaws in the specimen, preempting yielding. In any case, under tension the stress needed to induce yielding is at least  $\sim 6.5$  GPa, which is designated as the “yield strength” in tension. One may wonder if this asymmetry is due to tension-induced fertile sites for shear transformations<sup>16</sup>, causing some softening in the subsequent compression. Therefore, we also prepared independent tensile and compression samples, i.e., separate pillars for compression and “dog-bone shaped” samples for tension (see Methods section). For these samples, the measured strengths follow the same trend as that in TC samples: tensile excursion ends in fracture while compressive loading initiates homogeneous plastic flow at a much lower stress level (more data are documented in [Supplementary Fig. 2](#)). Fig. 1d summarizes the yield strength of a-Si ( $d = 110$  nm  $\sim 180$  nm) under compression (black) versus that under tension (red). We see that  $\sigma_T$  is considerably higher

than  $\sigma_c$ . In other words, we consistently observe that a-Si is much stronger in tension than in compression. Note that a-Si remained fully amorphous after either tensile or compressive deformation, as confirmed in post-mortem characterizations (Supplementary Fig. 3).

Dynamic tests in the apparent elastic regime provide further insight into the T-C asymmetry of a-Si. To achieve high sensitivity we used the nano dynamic mechanical analysis (nano-DMA) technique<sup>17,18</sup>. Stress-displacement curves were obtained by overlapping 10 loading-unloading cycles with peak stress well below the yielding strength. In the dynamic tensile tests, a-Si exhibits a linear elastic behavior for loading frequencies ranging from 0.5 Hz to 20 Hz, Fig. 2a. The push-to-pull device itself, in the absence of a-Si sample, also showed perfect linear elasticity (Supplementary Fig. 4). In contrast, the compressed a-Si exhibits a mechanical hysteresis loop, which expands gradually with increasing loading frequency. The energy dissipated can be assessed using the damping factor, which represents the ratio of the loss modulus to the storage modulus<sup>19</sup>. Storage modulus is a metric for the elastic energy stored in the sample; loss modulus, on the other hand, is a gauge of viscous response and measures the energy dissipated as heat<sup>20</sup>. The damping factor is found to be 0.009, 0.044, 0.105, 0.098 and 0.162, corresponding to the average strain rate of 0.05 s<sup>-1</sup>, 0.20 s<sup>-1</sup>, 0.51 s<sup>-1</sup>, 0.95 s<sup>-1</sup> and 1.82 s<sup>-1</sup>, respectively. Comparing tension versus compression in the nominally elastic regime, apparently a-Si is more elastic and stores more elastic strain energy under tension, whereas it undergoes much more anelastic relaxation with energy dissipation in compression. This T-C asymmetry in an elastic-dominant regime, i.e., anelasticity, is markedly enhanced under compression but suppressed under tension, and goes hand in hand with the asymmetry in yield strength.

### Atomistic simulations of the T-C asymmetry in a-Si

To corroborate the experimentally observed T-C asymmetry and shed light on the underlying mechanism, we have carried out molecular dynamics (MD) simulations using three different empirical potentials for a-Si, including the Stillinger-Weber (SW) potential<sup>21</sup>, an environment-dependent interatomic potential (EDIP)<sup>22</sup>, as well as a newly developed machine-learning (ML) interatomic potential<sup>23</sup>, which has been shown to generate atomic structure and properties close to the experimental measurements<sup>24</sup>. All these empirical potentials are

consistent in producing the T-C asymmetry. For conciseness, in the main text we only show the ML potential simulation results, whereas the results of SW and EDIP potentials are documented in Supplementary Information and Methods section with details about model preparation and deformation simulation.

We first simulated the uniaxial compression and tension of a-Si, in which the applied uniaxial load can be decomposed into shear stress  $\tau$  and normal stress  $\sigma_n$  on the maximum shear plane (inclined  $\sim 45^\circ$  to the loading axis), as schematically illustrated in Fig. 3a. The compressive yielding required a stress of  $\sim 5.5$  GPa at a strain of  $\sim 9\%$ , while the tensile yield strength is 7.2 GPa at a strain of 13%, Fig. 3b. Such a T-C asymmetry ( $\sigma_c < \sigma_t$ , also [Supplementary Figs. 5, 6](#)) is consistent with the experimental results in Fig. 1. The uniaxial tension and compression correspond to, respectively, positive (i.e.,  $\sigma_n > 0$ ) and negative (i.e.,  $\sigma_n < 0$ ) normal stress; the normal stress effect is therefore the key factor responsible for the T-C asymmetry. To provide quantitative information about the  $\sigma_n$  effect and remove the influence of free surface, we consider a deformation model of simple shear concurrent with a constant perpendicular normal stress  $\sigma_n$  (as illustrated in the right panel of Fig. 3a). Fig. 3c presents the shear stress-strain curves for ML a-Si in three  $\sigma_n$  cases (0 GPa, 3.5 GPa, -3.5 GPa). We observe that  $\sigma_n < 0$  leads to lowered yield strength, while  $\sigma_n > 0$  to increased yield strength, in conformity with the results presented earlier.

Next, we employed MD simulation to calculate the shear modulus  $G$  of a-Si at 300 K under different  $\sigma_n$  applied along the  $z$ -axis.  $G$  is examined here mainly because it is widely regarded as a key baseline property for amorphous materials, and known to be closely related to the energy barrier for shear transformation, yielding/flow, and structural relaxation, as shown for example in the cooperative shear model developed by Johnson and Samwer<sup>25</sup>. Fig. 3d shows the change of  $G_{xz}$  (or  $G_{yz}$ ) and  $G_{xy}$  as strain increases. Here the first and second subscript of  $G_{ij}$  represent the shear direction and normal direction of the shear plane, respectively (therefore  $G_{yz}$  is identical to  $G_{xz}$  considering the applied  $\sigma_n$  is along  $z$  axis). Since  $G_{xz}$  and  $G_{yz}$  are shear moduli in the plane normal to  $\sigma_n$ , they determine the energy barrier for shear events, under the tension or compression along the  $z$ -axis (resembling the uniaxial deformation illustrated in Fig. 3a). In early stages of straining, tensile normal stress ( $\sigma_n > 0$ ) increases  $G_{xz}$  (or  $G_{yz}$ ), which goes through a maximum value at large strains. In contrast, under compressive normal stress ( $\sigma_n <$

0),  $G_{xz}$  (or  $G_{yz}$ ) keeps decreasing from the get-go. The evolution of  $G_{xy}$  exhibits an opposite trend compared with  $G_{xz}$  and  $G_{yz}$ : the tensile normal stress leads to lower  $G_{xy}$ , while compressive stress increases  $G_{xy}$  slightly first and then reduces it. Therefore, the shear moduli become anisotropic when a normal stress is imposed on a-Si. This anisotropic variation/response of shear moduli, in turn, is partly responsible for the T-C asymmetry we have observed (see more explanations in Discussion part). The fourfold  $sp^3$ -bonded tetrahedra are the dominant local coordination motifs in a-Si ([Supplementary Fig. 7](#)). The analysis of orientational radial distribution function<sup>26</sup> ([Supplementary Fig. 8](#)) demonstrates that under tension and compression, the main structural change for those Si tetrahedra is the bonding anisotropy (as depicted by the elongated and shortened tetrahedra in Fig. 3e). As such, the normal-stress-sign-dependent response of shear moduli can be mainly attributed to this bonding anisotropy.

Besides shear modulus, we also take the coordination number (CN) change into consideration. An analysis of the fraction of a-Si atoms with CN=4 and CN>4 ([Supplementary Fig. 7](#)) shows that most atoms (over 90%) remain tetrahedral during deformation. The increase in the fraction of atoms with CN>4 is associated with deformation-induced fertile sites for shear transformations<sup>16,27</sup>, and the increased CN>4 sites under compression is higher than that under tension, especially in the plastic deformation regime, suggesting that compressive stress are more inclined to facilitate the local transformation from tetrahedral atomic environments to higher-coordinated, more fertile sites. Specifically, our deformation simulations under athermal quasi-static condition, in which the influence from thermal noise is absent, show that the fraction of Si atoms with non-affine squared displacement ( $D^2_{\min}$ )  $> 1 \times 10^{-4} \text{ \AA}^2$  (calculated with a constant strain offset of 0.01%) under compression is about twice that under tension (e.g.,  $\sim 3.1\%$  vs.  $\sim 1.5\%$  for tension and compression at the elastic strain of 0.02). This accounts for the T-C asymmetry in terms of anelasticity, since the origin of the nonlinear elasticity of amorphous solids rests in the liquid-like non-affine deformations<sup>28</sup>. We can also unify the anisotropic shear moduli at different normal stress (in both elastic and plastic regimes), by identifying a single structural parameter  $\lambda_{ij}$ . See [Supplementary Note 1](#) and [Supplementary Figs. 9-11](#) for details.

## Tension-compression asymmetry probed via resistance change

To verify the prediction about the CN change by simulations, we further carried out *in-situ* coupled mechanical-electrical tests inside TEM to measure the real-time electrical resistances of a-Si under tension and compression, respectively. If the shear deformations that locally convert the covalently-bonded and semiconducting tetrahedral environments into more metallic fertile motifs with  $\text{CN} > 4$ <sup>27,29,30</sup> are suppressed in tension but facilitated in compression, the resistivity change is expected to be different in tension and compression.

Fig. 4a shows the resistance change with time for a typical a-Si sample under tensile stress. Because the samples were loaded under a constant strain rate, the strain incurred is proportional to time under loading. The grey dashed line in Fig. 4a shows the calculated resistance change due to geometry change (see Supplementary Note 2, [Supplementary Figs.](#) 12, 13 and Table S1 for calculation details). The curve agrees well with the measured resistance, indicating that the observed resistance increase during tensile deformation arises entirely from sample elongation, and the resistivity stays constant. For compression, in contrast, the grey dashed curve shows the resistance reduction induced by pure geometry change of the a-Si pillar during the compressive flow does not agree with the measured resistance change (Fig. 4b). The difference between them, especially in the plastic deformation stage, indicates that the resistivity of a-Si decreased under compression. Such an observation is consistent with, and lends support to, the mechanism revealed by atomistic simulations (Fig. 3). That is, compressive normal stress serves to enhance the propensity for shear transformation events, which transform the semiconducting “solid-like” atomic environments into more metallic (conductive) and denser ones, decreasing the resistivity as a result. We also obtained evidence that shear transformations have indeed increased density (see Supplementary Note 3, [Supplementary Fig.](#) 14). In contrast, tension suppresses shear transformations, such that the sample experiences mainly elastic deformation, without producing much metallic and denser environments. This is manifested by the negligible change in resistivity demonstrated in Fig. 4a.

## Discussions

Our results, both experimental and computational, have shown two major contributing

factors to the extraordinary T-C asymmetry in a-Si. The first is the changes in the shear moduli, i.e., stiffening versus weakening, depending on the sign of the normal stress. This contribution comes into play even in the nominally elastic regime, as compression lowers the shear modulus and consequently the barrier against non-affine shear transformations that produce pronounced anelasticity. The other contribution is shear-transformation-induced densification or “liquefaction”, which converts local packing motifs into denser and more metallic-like environments that are easier to further deform; the electrical resistance change in Fig. 4 provides credence to this mechanism, which becomes more prevalent with increasing plastic strain.

Specifically, the shear modulus  $G$  signifies the magnitude of the activation barrier  $Q$  for shear transformation events; the lower the  $G$ , the higher propensity for shear transformations<sup>25</sup>, and vice versa. The normal-stress-sign-dependent  $G$  in a-Si thus goes hand in hand with the  $\sigma_n$  effect on  $Q$ , which can be described by:

$$Q = Q_0 - \tau \cdot \alpha_{\text{shear}} \Delta \varepsilon_{\text{shear}} \cdot V_{\text{initial}} - \sigma_n \cdot \alpha_{\text{volume}} \Delta V \quad (1)$$

where  $Q_0$  is the energy barrier of a shear event at room temperature without applied stress,  $V_{\text{initial}}$  is the initial volume of the zone before transformation,  $\Delta \varepsilon_{\text{shear}}$  and  $\Delta V \equiv V_{\text{final}} - V_{\text{initial}}$  are the local shear strain and volume variation of the final configuration with respect to the initial configuration, respectively. The dimensionless quantities  $\alpha_{\text{shear}}$ ,  $\alpha_{\text{volume}}$  describe the dependences of  $Q$  with respect to the shear stress  $\tau$  and normal stress  $\sigma_n$ , respectively. If the elastic modulus does not depend on stress,  $\alpha_{\text{shear}}$ ,  $\alpha_{\text{volume}}$  are simply the fraction of shear and dilation (or contraction) of the saddle-point configuration with respect to the entire (initial-to-final) transformation. But if it does,  $\alpha_{\text{shear}}$ ,  $\alpha_{\text{volume}}$  would absorb that additional effect as well.

For a-Si, the elementary shear transformation event turns a relatively open structure into a contracted one<sup>27,30,31</sup>. In other words, a local cluster of atoms undergoes rearrangement from the relatively low-energy configuration to a metastable one, crossing a transition state with higher coordination number ([Supplementary Fig. 15](#)) and a volume reduction, as evidenced by the atomistic calculation of Boioli *et al.*<sup>32</sup>. With the supercell held fixed, they studied how the supercell pressure varies along the transition path: a negative pressure variation means a negative volume change (densification) of the transformation zone. As  $\Delta V$  is negative for a-Si,

and  $\alpha_{\text{volume}}$  is a positive value, the sign of  $\sigma_{\text{n}}$  makes the difference observed in our experiment. [Supplementary Fig. 16](#) schematically shows the resultant  $Q$  dependence on strain under tension and compression, reminiscent of the trends with the  $G_{xz}$  (or  $G_{yz}$ ) evolution in Fig. 3d. The consequence is that compression lowers shear modulus and the energy barrier, so the transition state is easier to be crossed, leading to easier pop-ups of shear transformation events. This instigates yielding at a lower stress, followed by strain softening (see the true stress-strain curve in [Supplementary Fig. 17](#)). In contrast, tension makes the shear events more difficult to be activated such that the yield strength can reach a quite high value if flaw-induced premature fracture does not set in<sup>7</sup>. All in all, a-Si is stronger under tension but more “ductile” under compression.

Importantly, such an extraordinary T-C asymmetry may exist in other amorphous materials with similar tetrahedral structures:  $\sigma_{\text{c}} < \sigma_{\text{T}}$  is also found in our MD simulations of a-Ge and a-SiO<sub>2</sub> (silica glass), see [Supplementary Fig. 18](#). It could be a unique property of open-framework covalently bonded glasses. For the metallic glasses (MGs) samples with similar dimensions, on the other hand, their  $\sigma_{\text{T}}$  is slightly lower than  $\sigma_{\text{c}}$  (see [Supplementary Fig. 19](#)). This is because, unlike the open structure of a-Si<sup>33</sup>, MGs are densely packed with CN on the order of 12 due to the non-directional metallic bonding<sup>34</sup>, and their atomic shuffle in shear transformations causes volume expansion rather than shrinkage at the saddle-point<sup>35</sup>. This distinction has a similar origin as the density anomaly in the melting of ice, which is lighter than liquid water, yet more shear-rigid and less diffusively mobile. The saddle-point states of the shear-diffusion transformation zone<sup>36</sup> by definition need to be less shear-rigid and more diffusively mobile than the starting state. Such trend could be generic in tetrahedrally coordinated solids<sup>37</sup>.

T-C asymmetry is critical for a-Si microelectronics or microelectromechanical systems (MEMS) devices that serve under tension-compression cyclic loading. The stress sign dependent modulus and energy barrier we proposed here, together with the strain-stiffening mechanism found in cementite, biological materials, elastomers<sup>38</sup> etc., may inspire us to invent new materials with novel elastic properties. For small-scale a-Si devices, an unusually high yield strength and large yield strain may be desirable and can be achieved if the structure component is designed to be under tensile loading. Certainly, the higher tensile stress would

eventually cause brittle failure. It has been reported that increasing hydrogen content will mitigate the brittleness in tensile stress state<sup>39-41</sup>. Also, lithiated Si (SiLi<sub>x</sub>) is of great application interest as anode in Li-ion battery. At heavy degree of lithiation, the open-framework structure of silicon collapses, and the atomic structure is more akin to metallic glass. Correspondingly, it was found that a hydrostatic compressive stress strengthens the lithiated Si, while a hydrostatic tensile stress promotes its plasticity<sup>42</sup>. Therefore, it will be of interest to experimentally explore the chemical modulation of T-C asymmetry in a-Si.

## Conclusion

In summary, through quantitative tension and compression testing of submicron-scale specimens, as well as detailed MD simulations, we have uncovered an extraordinary and pronounced tension-compression asymmetry in a-Si. First, the yield strength in tension is considerably higher than that in compression. The asymmetry in yield strength can be explained by the “normal stress sign effect” on the shear moduli and thus activation energy barrier for the elementary shear event — shear transformations, which carry both the anelastic and plastic events. Compression lowers the activation barrier of shear transformations to facilitate yielding, whereas tension increases the activation barrier energy, rendering the activation of shear transformations more difficult and thus requiring a larger resolved shear stress. Second, in the nominally elastic regime, a hysteresis loop associated with the non-affine deformation appears only in compression. Third, the coupled mechanical-electrical tests revealing electrical resistivity changes have provided a sensitive indicator of the structural change underlying the T-C asymmetry: shear transformations have indeed been activated in compression but not in tension, switching semiconducting motifs to more metallic- and denser, liquid-like ones. The hitherto unheralded asymmetry discovered in this work is expected to hold for other materials similar to a-Si. In general, our findings provide insights for understanding the intrinsic response of open-framework glasses to different stress states. They may also be of practical relevance to the utility of small-scale a-Si in microelectronics and microelectromechanical systems.

## References

1. Meyers, M. A., Chawla, Krishan Kumar. *Mechanical behavior of materials (Second Edition)*, (Cambridge University Press, 2008).
2. Chen, X., Wu, Shengxing, Zhou, Jikai. Influence of porosity on compressive and tensile strength of cement mortar. *Constr. Build. Mater.* **40**, 869-874 (2013).
3. Pelleg, J. *Mechanical properties of ceramics*. Vol. 213 (Springer Science & Business, 2014).
4. Wachtman, J. B., Cannon, W. R., Matthewson, M. J. *Mechanical properties of ceramics*. (John Wiley & Sons, 2009).
5. Davidge, R. Mechanical properties of ceramic materials. *Contemp. Phys.* **10**, 105-124 (1969).
6. Griffith, A. The phenomena of flow and rupture in solids. *Phil Trans. Roy. Soc., A* **221**, 163-198 (1920).
7. Zhao, P., Li, Ju, Wang, Yunzhi,. Extended defects, ideal strength and actual strengths of finite-sized metallic glasses. *Acta Mater.* **73**, 149-166 (2014).
8. Zhang, H. *et al.* Approaching the ideal elastic strain limit in silicon nanowires. *Sci. Adv.* **2**, e1501382 (2016).
9. Banerjee, A. *et al.* Ultralarge elastic deformation of nanoscale diamond. *Science* **360**, 300-302 (2018).
10. Tian, L. C., Y. Q. Shan, Z. W. *et al.* Approaching the ideal elastic limit of metallic glasses. *Nature Commun.* **3**, 609 (2012).
11. Hedler, A., Klaumünzer, Siegfried Ludwig, Wesch, Werner. Amorphous silicon exhibits a glass transition. *Nat. Mater.* **3**, 804 (2004).
12. Treacy, M., Borisenko, K. B. The local structure of amorphous silicon. *Science* **335**, 950-953 (2012).
13. Wang, Y. *et al.* Tunable Anelasticity in Amorphous Si Nanowires. *Nano Lett.* **20**, 449-455, (2020).
14. S. Sriraman, S. Agarwal, E. S. Aydil, D. Maroudas, Mechanism of hydrogen-induced crystallization of amorphous silicon. *Nature* **418**, 62-65 (2002).
15. Deringer, V. L. B. *et al.* Origins of structural and electronic transitions in disordered silicon. *Nature* **589**, 59-64 (2021).
16. Gerbig, Y. B., Michaels, C. A., Bradby, J. E., Haberl, B. & Cook, R. F. In situ spectroscopic study of the plastic deformation of amorphous silicon under nonhydrostatic conditions induced by indentation. *Phys. Rev. B* **92**, 214110 (2015).
17. Liu, K., Ostadhassan, Mehdi, Bubach, Bailey, Dietrich, Robert, Rasouli, Vamegh. Nano-dynamic mechanical analysis (nano-DMA) of creep behavior of shales: Bakken case study. *J. Mater. Sci* **53**, 4417-4432 (2018).
18. Ye, J. C., Lu, J. Liu, C T, Wang, Q. Yang, Y. Atomistic free-volume zones and inelastic deformation of metallic glasses. *Nat. Mater.* **9**, 619-623 (2010).
19. Herbert, E., Oliver, WC, Pharr, GM. Nanoindentation and the dynamic characterization of viscoelastic solids. *J. Phys. D: Appl. Phys.* **41**, 074021 (2008).
20. Yuan, Y., Verma, Ritu. Measuring microelastic properties of stratum comeum. *Colloids Surf. B Biointerfaces* **48**, 6-12 (2006).
21. Stillinger, F. H. & Weber, T. A. Computer simulation of local order in condensed phases of silicon. *Phys. Rev. B* **31**, 5262 (1985).
22. Justo, J. F., Bazant, M. Z., Kaxiras, E., Bulatov, V. V., Yip, S. Interatomic potential for silicon defects and disordered phases. *Phys. Rev. B* **58**, 2539 (1998).
23. Bartok, A. P., Kermode, J. R., Bernstein, N. & Csanyi, G. Machine Learning a General-Purpose Interatomic Potential for Silicon. *Phys. Rev. X* **8** (2018).
24. Deringer, V. L., *et al.* Realistic Atomistic Structure of Amorphous Silicon from Machine-Learning-Driven Molecular Dynamics. *J. Phys. Chem. Lett.* **9**, 2879-2885 (2018).

25. Johnson, W., Samwer, Konrad. A universal criterion for plastic yielding of metallic glasses with a  $(T/T_g)^{2/3}$  temperature dependence. *Phys. Rev. Lett.* **95**, 195501 (2005).

26. Fan, Z., Ma, E. Predicting orientation-dependent plastic susceptibility from static structure in amorphous solids via deep learning. *Nature Commun.* **12**, 1506 (2021).

27. Demkowicz, M. J., Argon, A. S. High-density liquidlike component facilitates plastic flow in a model amorphous silicon system. *Phys. Rev. Lett.* **93**, 025505 (2004).

28. Rubinstein, M., M. Panyukov. Nonaffine deformation and elasticity of polymer networks. *Macromolecules* **30**, 8036-8044 (1997).

29. Argon, A., Demkowicz, M. What can plasticity of amorphous silicon tell us about plasticity of metallic glasses? *Metall. Mater. Trans. A* **39**, 1762-1778 (2008).

30. Demkowicz, M. J., Argon, A. S. Liquidlike atomic environments act as plasticity carriers in amorphous silicon. *Phys. Rev. B* **72**, 245205 (2005).

31. Fan, Z., Ding, Jun, Li, Qing Jie, Ma, Evan. Correlating the properties of amorphous silicon with its flexibility volume. *Phys. Rev. B* **95** (2017).

32. Boioli, F., Albaret, T., Rodney, D. Shear transformation distribution and activation in glasses at the atomic scale. *Phys. Rev. E* **95**, 033005 (2017).

33. Morishita, T. High density amorphous form and polyamorphic transformations of silicon. *Phys. Rev. Lett.* **93**, 055503 (2004).

34. Cheng, Y., Ma, E. Atomic-level structure and structure–property relationship in metallic glasses. *Prog. Mater. Sci.* **56**, 379-473 (2011).

35. Schuh, C. A., Lund, A. C. Atomistic basis for the plastic yield criterion of metallic glass. *Nat. Mater.* **2**, 449-452 (2003).

36. Li, W., Rieser, Jennifer M, Liu, A. J., Durian, D. J., Li, J. Deformation-driven diffusion and plastic flow in amorphous granular pillars. *Phys. Rev. E* **91**, 062212 (2015).

37. Daisenberger D, M. P. F., Wilson M. Crystal-liquid interfaces and phase relations in stable and metastable silicon at positive and negative pressure. *Phys. Rev. B* **82**, 214101 (2010).

38. Jiang, C., Srinivasan, S. G. Unexpected strain-stiffening in crystalline solids. *Nature* **496**, 339-342 (2013).

39. Johlin, E. *et al.* Structural origins of intrinsic stress in amorphous silicon thin films. *Phys. Rev. B* **85** (2012).

40. Gaire C, Y. D. X., Lu T M, G. C. Wang, R. C. Picu. Deformation of amorphous silicon nanostructures subjected to monotonic and cyclic loading. *Journal of Materials Research. J. Mater. Res.* **23**, 328-335 (2008).

41. Abadias G. *et al.* Review Article: Stress in thin films and coatings: Current status, challenges, and prospects. *J. Vac. Sci. Technol. A* **36**, 020801 (2018).

42. Zhao, K. J., Li, Y. G., Brassart, L. Pressure-sensitive plasticity of lithiated silicon in Li-ion batteries. *Acta Mech. Sinica* **29**, 379-387 (2013).

## Methods

### Deposition of the a-Si Film by PECVD

For simplicity of submicron-sized mechanical samples' preparation, a-Si film was deposited on an  $<001>$  oriented and wedge-shaped single-crystalline Si substrate with the  $\sim 8$   $\mu\text{m}$  top width (Supplementary Fig. 1a). Amorphous Si film was prepared using a plasma enhanced chemical vapor deposition (PECVD) method with the radio frequency (RF) power of 20 W, at

250 °C substrate temperature, 800 mTorr process pressure, pure SiH<sub>4</sub> flow rate of 30 sccm, and Ar flow rate of 475 sccm. The thickness of the a-Si film is about 11  $\mu$ m. The deposited a-Si film adhered firmly to the substrate surface, and no obvious voids have been found during the FIB milling process. The a-Si samples machined from the a-Si film have a uniform microstructure (Supplementary Fig. 1).

### **Samples preparation for nanomechanical tests**

A-Si pillars and tensile samples used in this work were microfabricated from the deposited parent body of a-Si film, using focused ion beam (FEI Helios NanoLab 600 dual-beam FIB system) under a 30 kV accelerating voltage. The beam current of Ga ions sequentially decreased from 9.3 nA (coarse cutting) to 1.5 pA (fine polishing). Typical examples of the FIB-fabricated a-Si pillar and tensile sample (including the corresponding gripper, inset) are shown in Supplementary Fig. 3. The effective size  $d$  is defined as the nominal diameter measured at the half height of pillars. The effective size  $d$  of the tensile samples is calculated by  $d = \sqrt{A}$ , where  $A$  is the measured cross-sectional area after brittle fracture.

### ***In-situ* quantitative mechanical tests in TEM**

A-Si samples were compressed or tensioned under uniaxial loading performed by the Hysitron PI95 TEM PicoIndenter inside a JEOL JEM 2100F TEM at 200 keV. The engineering stress was defined as the ratio of the measured load to the nominal cross-sectional area  $A$  of specimens, and the engineering strain  $\varepsilon$  was calculated to be the ratio of deformation displacement to the initial height  $h$  of pillars or initial length  $l$  of tensile samples. All *in-situ* mechanical tests were carried out under the displacement control mode by changing the loading rate to keep a roughly constant strain rate for different samples. The strain rates for all tests were in the range of 1~5  $\times 10^{-3}$  s<sup>-1</sup> (quasi-static loading). The tensile and compressive tests were performed under comparable electron beam illumination.

### **Dynamic tensile and compressive tests**

To ensure ultrahigh mechanical sensitivity in the dynamic tests, the Hysitron NanoIndenter

system (Hysitron TI950) equipped with a NanoDMA module, was employed. After calibration, the achievable resolutions of the nanoindentation system in displacement and in load are  $\sim 1$  nm and  $\sim 1$   $\mu$ N, respectively. A-Si pillars used for dynamic compressive tests were also fabricated by FIB in the same way as mentioned above. The tensile samples were lifted-out from the pre-thinned a-Si lamellae using a piezoelectric micromanipulator (Kleindiek nanotechnik, Germany) and then positioned on a MEMS-based push-to-pull (PTP) device. The tensile sample was aligned carefully perpendicular to the trench edge to secure the uniaxial loading condition, and the both ends were welded via ion-beam induced Pt deposition. The whole process was performed inside a dual beam FIB System (FEI Helios 600 NanoLab). To avoid fracture or plastic deformation, the nominal cyclic stress was set to be far less than the fracture strength or yield strength. To ensure the data reproducibility, 10 loading cycles were applied for each run of the dynamic tests. The spectrum of each load cycle is of a triangular shape, consisting of symmetrical loading and unloading portions. It was found that 10 loading cycles were sufficient to achieve a steady-state dynamic response in our present experimental setup.

## MD simulations

The a-Si model containing 8,192 atoms using ML potential was generated following a quench protocol similar to that in Ref.<sup>24</sup>, with sample dimensions of  $4.5$  nm  $\times$   $4.3$  nm  $\times$   $8.7$  nm in  $x$ ,  $y$  and  $z$  direction, respectively. Stress-strain curves for uniaxial tension and compression along  $z$  direction were obtained from samples with free surface in the  $x$  direction and periodic boundary conditions (PBC) in  $y$  and  $z$  directions. All molecular dynamic simulations were implemented in LAMMPS<sup>43</sup>. The time step used in all simulations was 1 fs. ML-modeled a-Si was produced by heating a supercell of diamond silicon composed of  $8$  (X)  $\times$   $8$  (Y)  $\times$   $16$  (Z) unit cells to 2800 K into equilibrium liquids. Then it was quenched to 300 K with the effective cooling rate of  $1 \times 10^{11}$  K/s, following the similar protocol as that in Ref<sup>24</sup>. The a-Si samples using SW and EDIP potentials contain 640,000 atoms and were prepared with the cooling rate of  $1 \times 10^{12}$  K/s. All those quenching and equilibrations were conducted in the NPT ensemble under a Nose-Hoover thermostat with zero external pressure. The periodic boundary condition was applied in all three directions.

The deformation of a-Si samples was conducted at 300 K with the applied strain rate of  $1 \times 10^9$  s $^{-1}$  for ML potential as well as  $1 \times 10^7$  s $^{-1}$  for SW and EDIP potentials. At different degree of strain, the shear modulus  $G_{i,j}$  along different orientations (i.e.,  $\pm xy$ ,  $\pm xz$ ,  $\pm yz$ , and we use the average value of  $G_{+i,j}$  and  $G_{-i,j}$  as the value of  $G_{i,j}$ ) of a-Si models was derived from the shear stress-strain curves at small (1.0%) strain. The vibrational mean squared displacement (MSD $_i$ ) of a single atom along  $i$  direction is defined as  $\langle [x_i(t) - \bar{x}_i]^2 \rangle$ , where  $\bar{x}_i$  is the equilibrium (time-averaged) position of the atom along  $i$  direction, and the MSD is evaluated on short time scales when the MSD is flat with time and thus contains the vibrational but not the diffusional contribution<sup>44</sup>. The calculated MSD was taken by averaging over 100 independent runs, all starting from the same configuration but with momenta assigned randomly from the appropriate Maxwell-Boltzmann distribution.

## References

43. Plimpton, S. Fast parallel algorithms for short-range molecular dynamics. *J. Comput. Phys.* **117**, 1-19 (1995).
44. Ding, J. *et al.* Universal structural parameter to quantitatively predict metallic glass properties. *Nature Commun.* **7**, 13733 (2016).

## Acknowledgements

Z.W. S. and Y.C.W. acknowledge support from National Natural Science Foundation of China (51902249 and 5203000210), the National Key Research and Development Program of China (No.2017YFB0702001) and China Postdoctoral Science Foundation (2019M663696). J.D. acknowledges the support from National Natural Science Foundation of China (12004294) and National Youth Talents Program. J.L. acknowledges the support by National Science Foundation (DMR-1923976). L.T. acknowledges the Alexander von Humboldt Foundation and the Start-Bridge-Finish Program from ICASEC for financial support. Z.F. thanks Albert Bartok-Partay for the help in using the machine-learning-based interatomic potential, and acknowledges the computational resources of the Maryland Advanced Research Computing Center (MARCC). The authors thank Jianxue Zhu, Songyu Yan and Danli Zhang at Xi'an Jiaotong University (XJTU) for their assistance in nano-DMA tests. E.M. and J.D. acknowledge XJTU for supporting their work at CAID.

## Author contributions

E.M., J.L. and Z.W.S. supervised the project. Y.W. and L.T. carried out the experimental investigations with assistance from M.L., H.L. and Y.Z. J.D. and Z.F. led the modeling effort. E.M. and Y.W. wrote the paper with input from J.D., Z.F., J.L. and Z.W. All authors contributed to the discussions.

## Competing interests

The authors declare no competing interests.

**Data availability.** The source data for Figs. 1–4 are attached. Additional data reported in the Supplementary Information are available from the corresponding authors upon request.

**Code availability.** The computer codes are available from the corresponding authors upon reasonable request.

## Figures captions

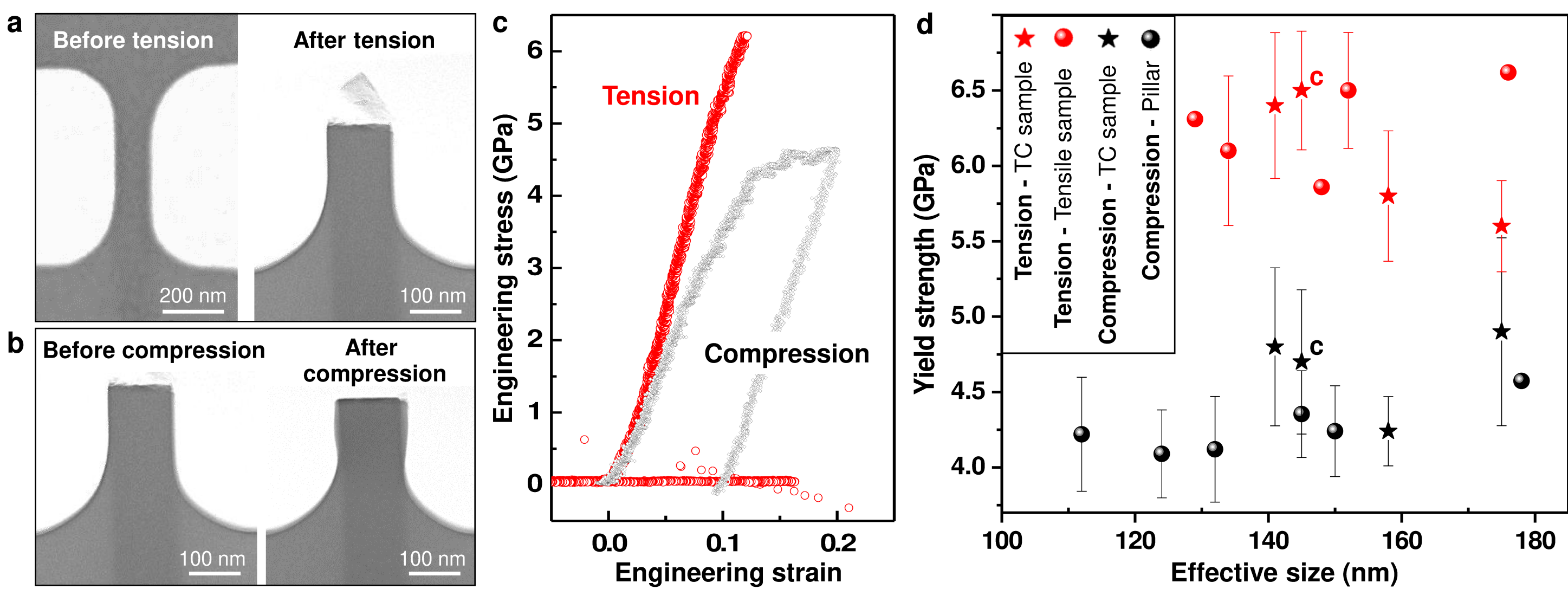
**Fig. 1 | Tension-compression asymmetry in submicron-sized a-Si.** **a**, The gauge section of a typical tension-compression (TC) a-Si sample before test (left), and after its brittle fracture in the tensile test (right). **b**, Subsequent compression test on the left-over sample section. **c**, Engineering stress-strain curves of the TC sample under tension (red) and compression (black). **d**, Tensile and compressive yield strength of a-Si samples with the effective size of 100~200 nm. The error bar encloses twice the standard deviation.

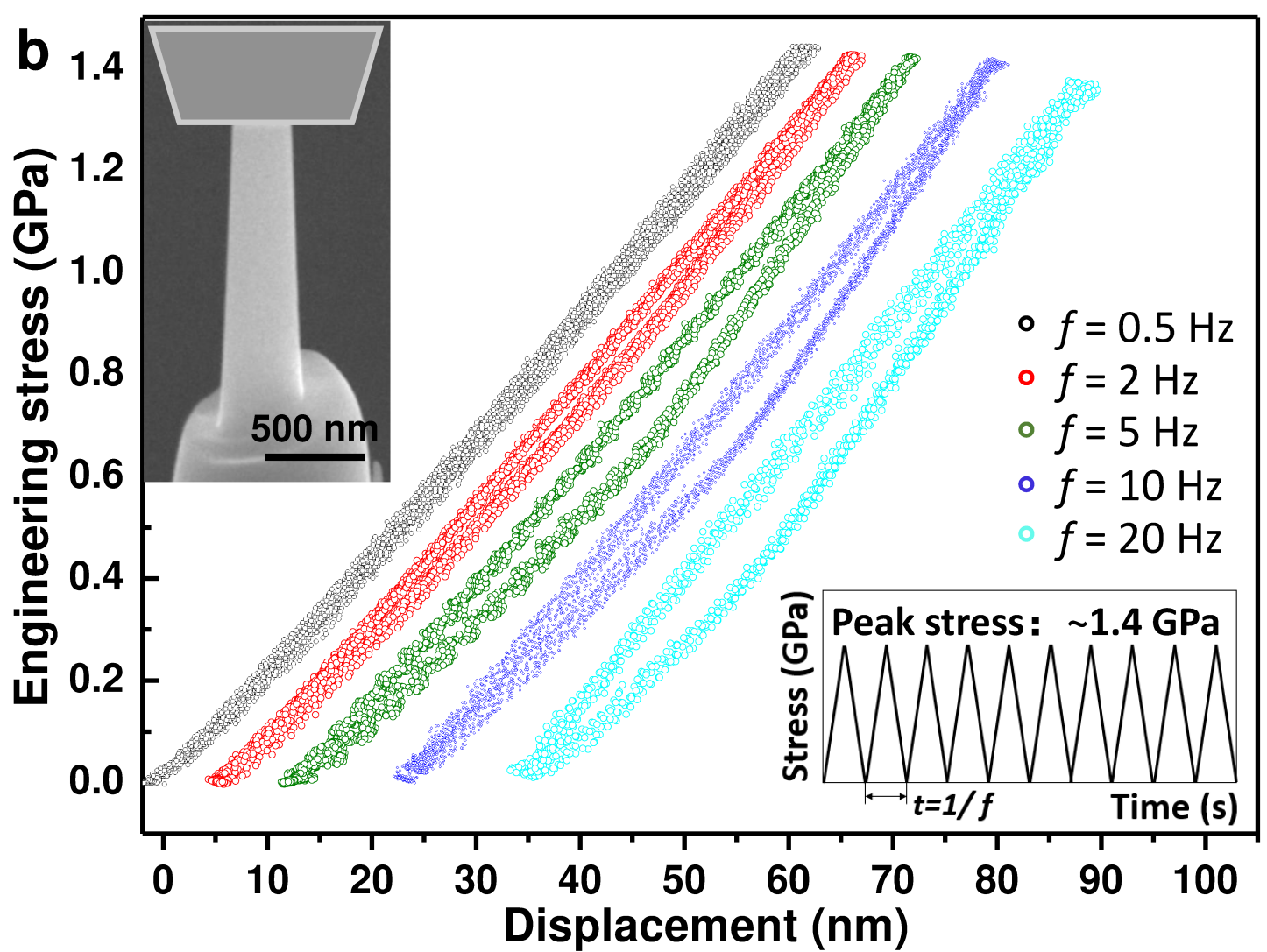
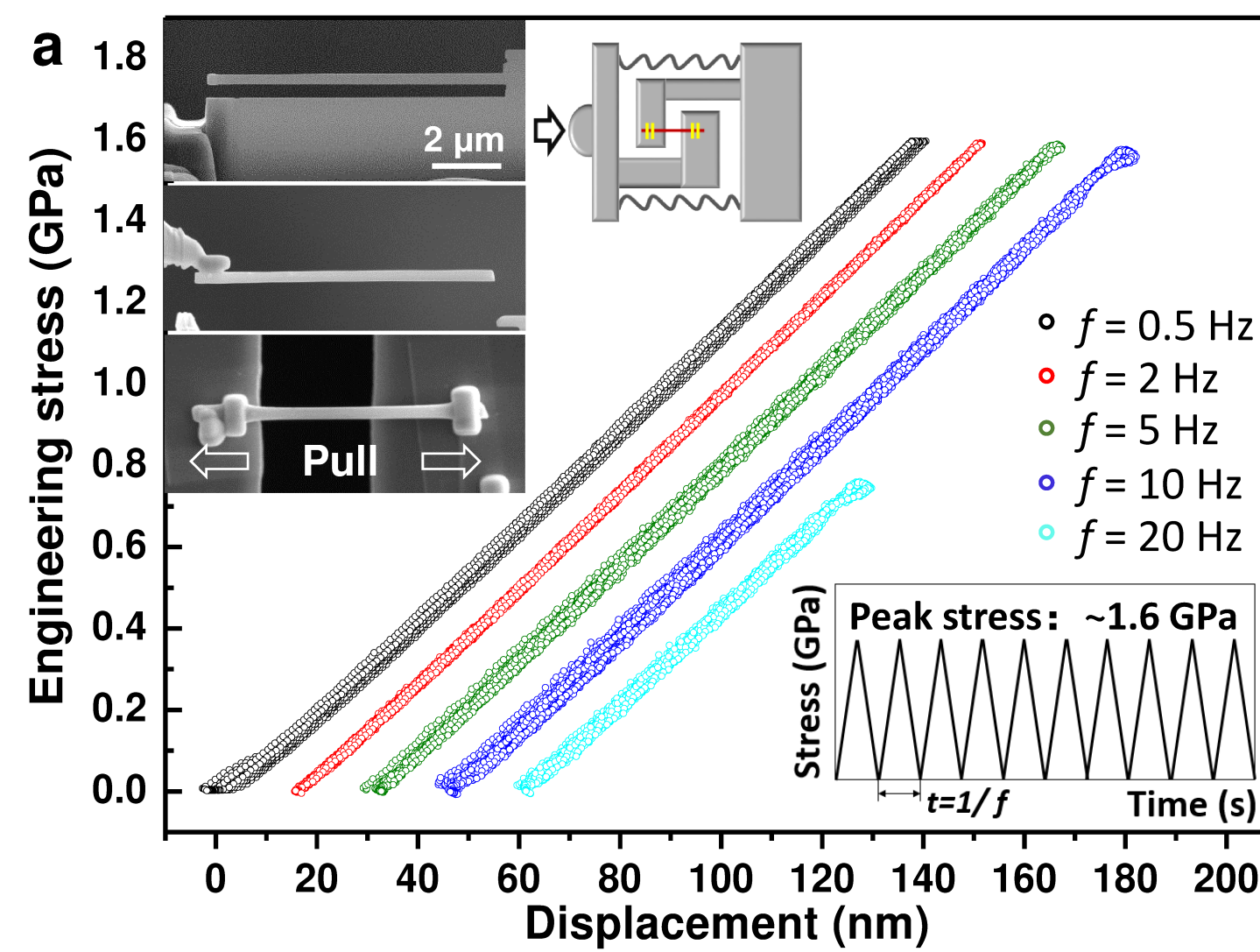
**Fig. 2 | Tension-compression asymmetry of submicron-sized a-Si in the nominally “elastic” regime.** **a**, The load-displacement curves obtained by cycling an a-Si tensile sample 10 times at different load-unload frequencies. The left insets show that the a-Si tensile sample was thinned and cut by FIB, transferred to a push-to-pull device, and then fixed using Pt deposition on both ends. The lower right corner inset shows the triangular-shaped loading cycles, consisting of symmetrical loading and unloading portions. **b**, The load-displacement curves obtained by cycling an a-Si pillar under compression 10 times at different load cycle frequencies. The upper left inset shows the SEM image of the pillar after test. The lower right corner inset shows the triangular-shaped loading cycles.

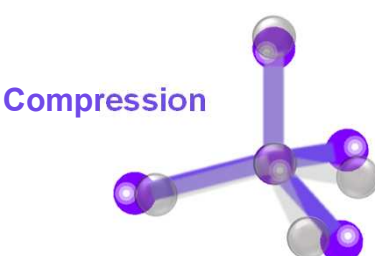
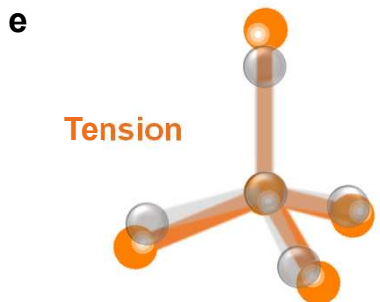
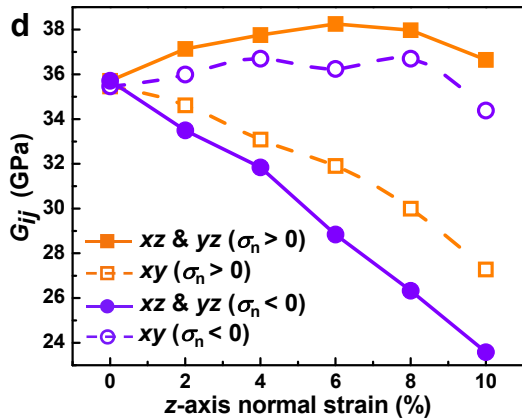
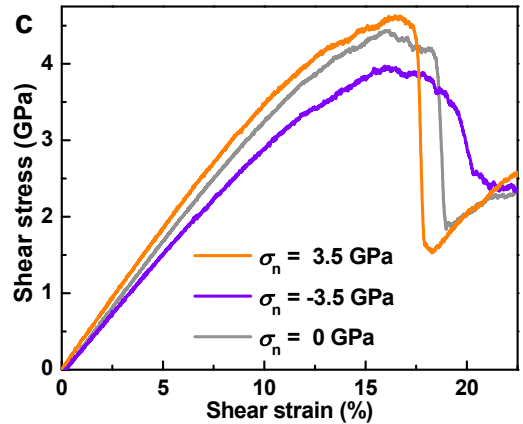
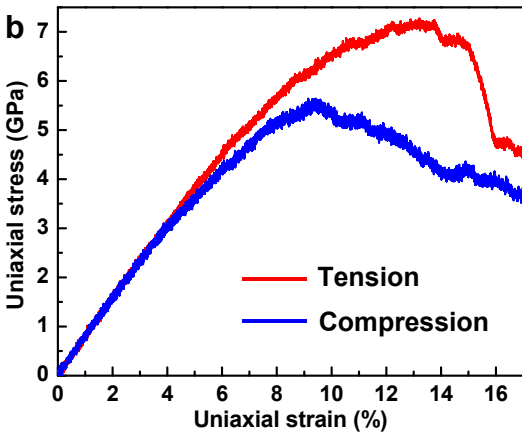
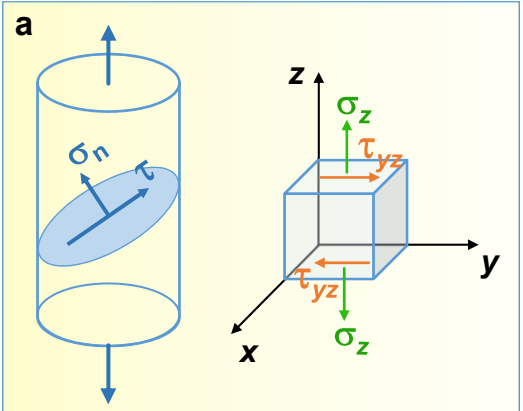
**Fig. 3 | MD simulations of the T-C asymmetry in a-Si.** **a**, Schematic showing uniaxial deformation (left panel) as well as simple shear deformation with simultaneously imposed perpendicular normal stress (right). **b**, Uniaxial tension and compression stress-strain curves along the  $z$ -axis at 300 K for ML a-Si model with free surface in the  $x$ -direction (periodic boundary condition, PBC in  $y$  and  $z$  directions). **c**, Stress-strain curve for simple shear deformation in  $xz$  direction, simultaneously with applied normal stress  $\sigma_n$  (in the  $z$ -direction)

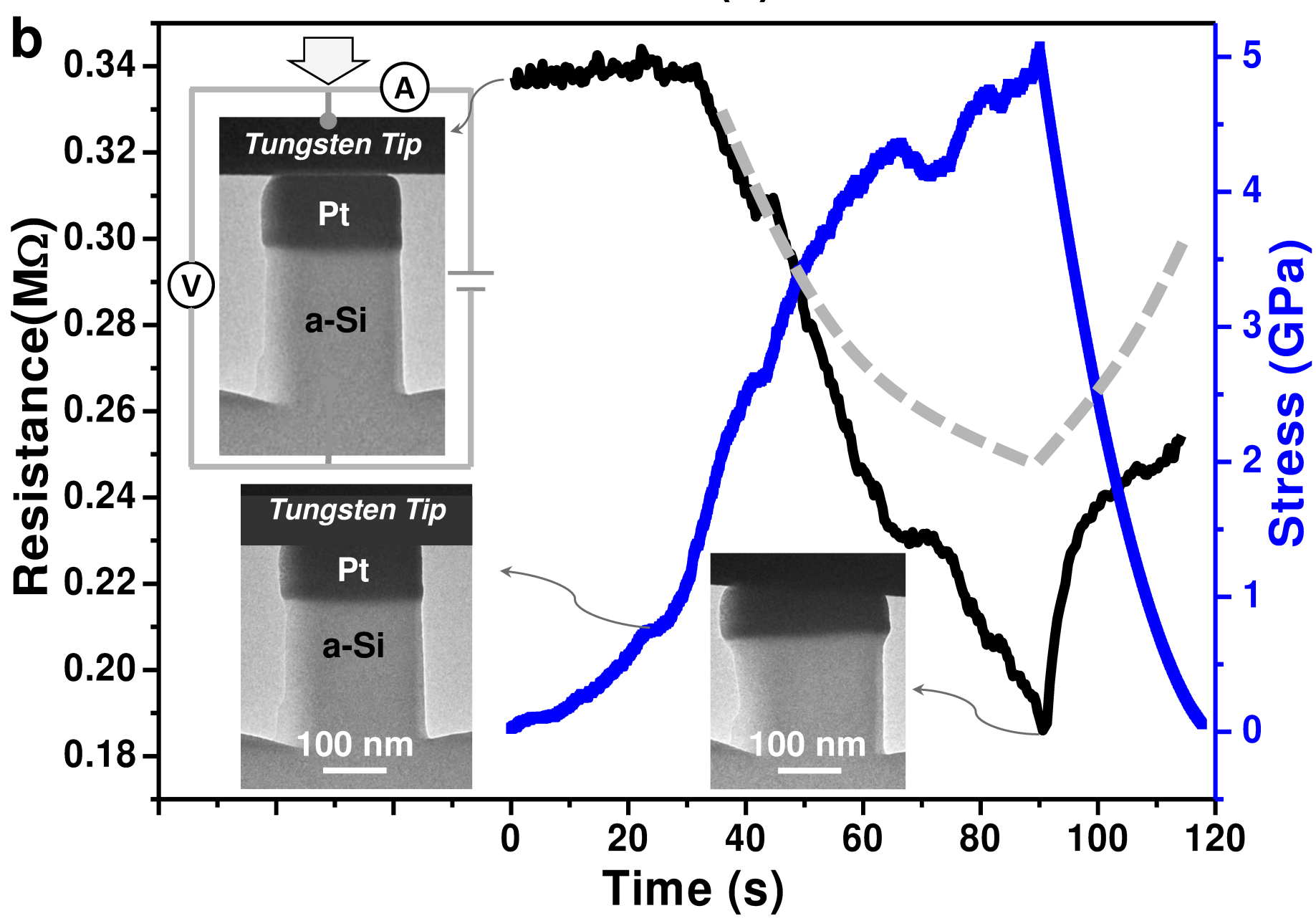
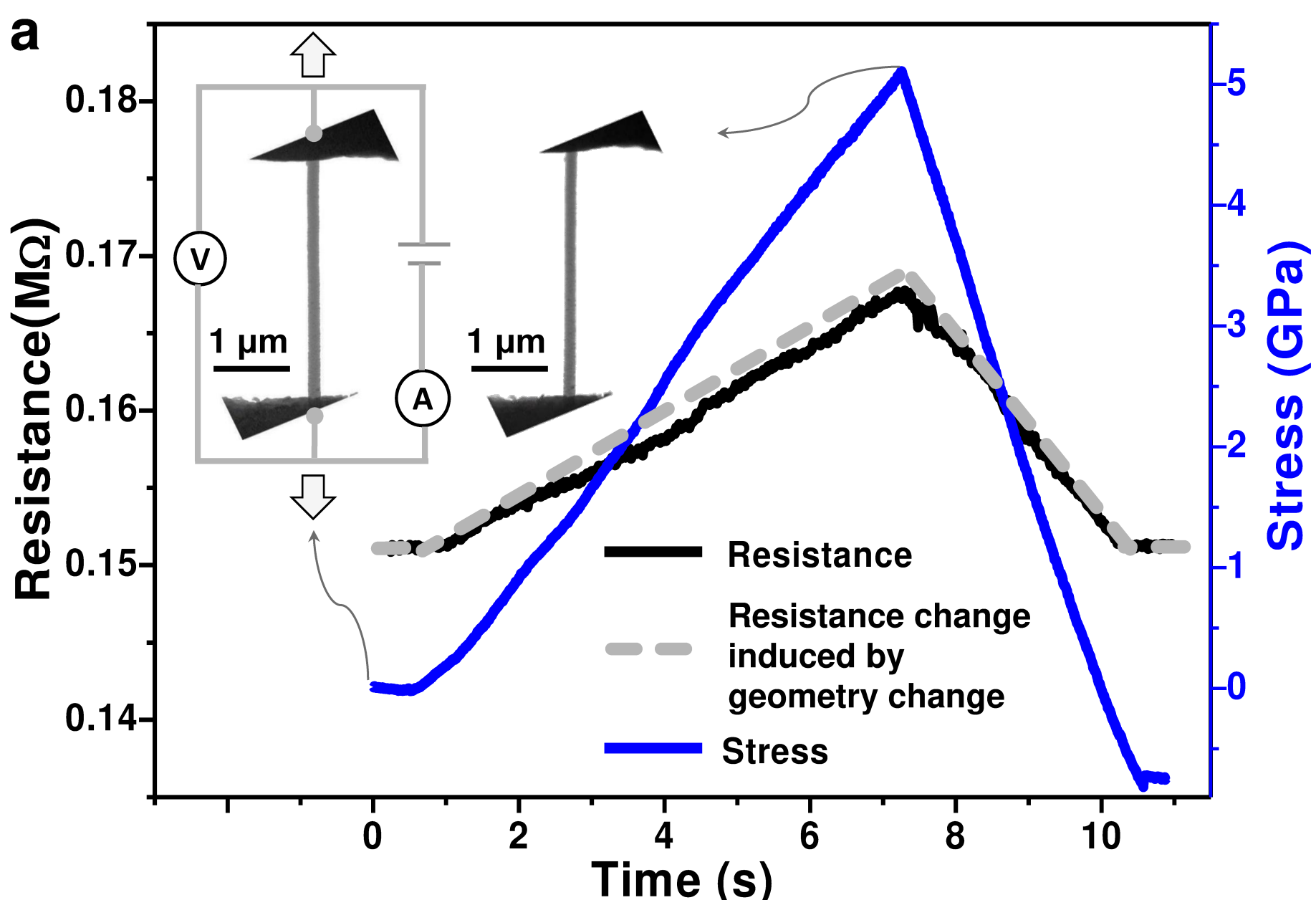
in ML a-Si model (PBC in all three dimensions). **d**, Effects of normal stress ( $\sigma_n$  in the  $z$  direction) on the shear moduli  $G_{xz}$  (and  $G_{yz}$ ) and  $G_{xy}$  of ML a-Si at 300 K. **e**, Typical relative rearrangements of the tetrahedral packing under tension and compression. The a-Si tetrahedron in gray is its unstrained state.

**Fig. 4 | Electrical resistance measured for a-Si under tension versus compression.** **a**, Stress excursion (blue curve) and corresponding resistance (black curve) as a function of time in tensile test. The inset shows the experimental setup and the tensile sample in its initial and final state. **b**, Stress excursion and corresponding resistance as a function of time in compression test. The insets show the experimental setup and the morphology of the compressed pillar at different states.









# Supplementary Information

## for

### Tension-compression asymmetry in amorphous silicon

Yuecun Wang<sup>1\*</sup>, Jun Ding<sup>2\*</sup>, Zhao Fan<sup>3\*</sup>, Lin Tian<sup>4\*</sup>, Meng Li<sup>1</sup>, Huanhuan Lu<sup>1</sup>, Yongqiang Zhang<sup>1</sup>, En Ma<sup>2†</sup>, Ju Li<sup>5†</sup>, Zhiwei Shan<sup>1†</sup>

<sup>1</sup>*Center for Advancing Materials Performance from the Nanoscale (CAMP-Nano) & Hysitron Applied Research Center in China (HARCC), State Key Laboratory for Mechanical Behavior of Materials, Xi'an Jiaotong University, Xi'an 710049, China*

<sup>2</sup>*Center for Alloy Innovation and Design (CAID), State Key Laboratory for Mechanical Behavior of Materials, Xi'an Jiaotong University, Xi'an 710049, China*

<sup>3</sup>*Department of Materials Science and Engineering, Johns Hopkins University, Baltimore, Maryland 21218, USA*

<sup>4</sup>*Institute of Materials Physics, University of Göttingen, Niedersachsen 37077, Germany*

<sup>5</sup>*Department of Nuclear Science and Engineering, and Department of Materials Science and Engineering, Massachusetts Institute of Technology, Cambridge, Massachusetts 02139, USA.*

This document contains Supplementary Figures (Fig. SI 1-19), Supplementary Notes (1-3), Supplementary Table and additional references (1-18).

Supplementary Video: *In-situ* TEM video shows the tension and compression processes of a representative a-Si TC sample.

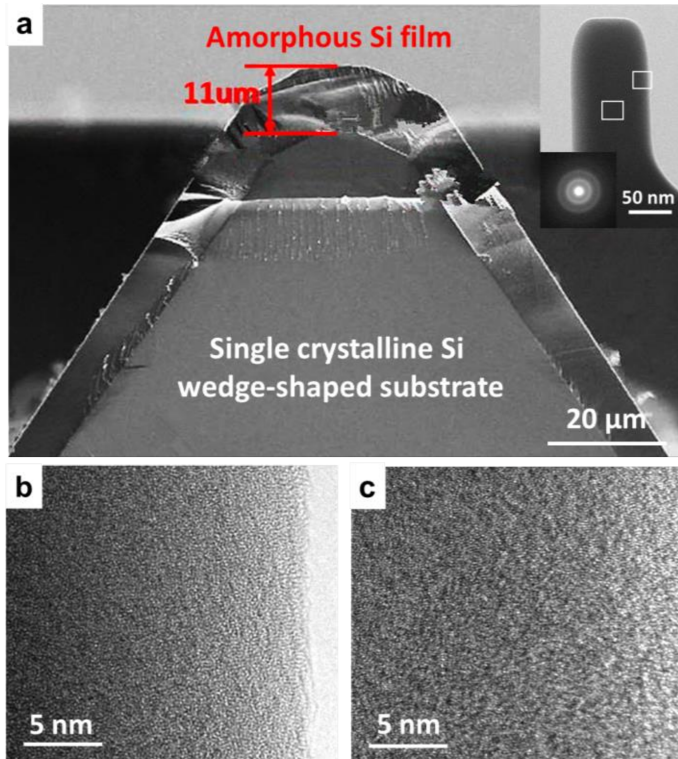


**Fig. SI-1 | Sample information.** (a) Cross-sectional SEM image of the deposited a-Si film on a wedge-shaped single-crystalline Si substrate. The thickness of the a-Si film (~11  $\mu\text{m}$ ) is large enough for fabricating the submicron-sized a-Si pillars using FIB. The inset shows the TEM image and electron diffraction pattern of an as-fabricated a-Si pillar. High-resolution TEM images of the white-boxed zones in the inset in (a), near the edge (b) and near the center (c) of the pillar. The diffraction halo and the maze-like feature of the phase-contrast in TEM images verify that the FIB-fabricated a-Si sample is fully amorphous without any visible crystalline phase.

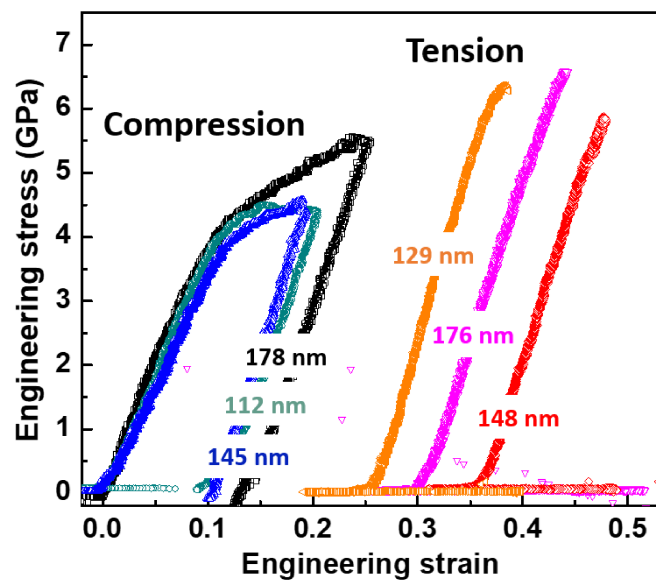


**Fig. SI-2** | Typical engineering stress-strain curves of submicron a-Si pillars under compression (left) and dog-bone samples under tension (right).

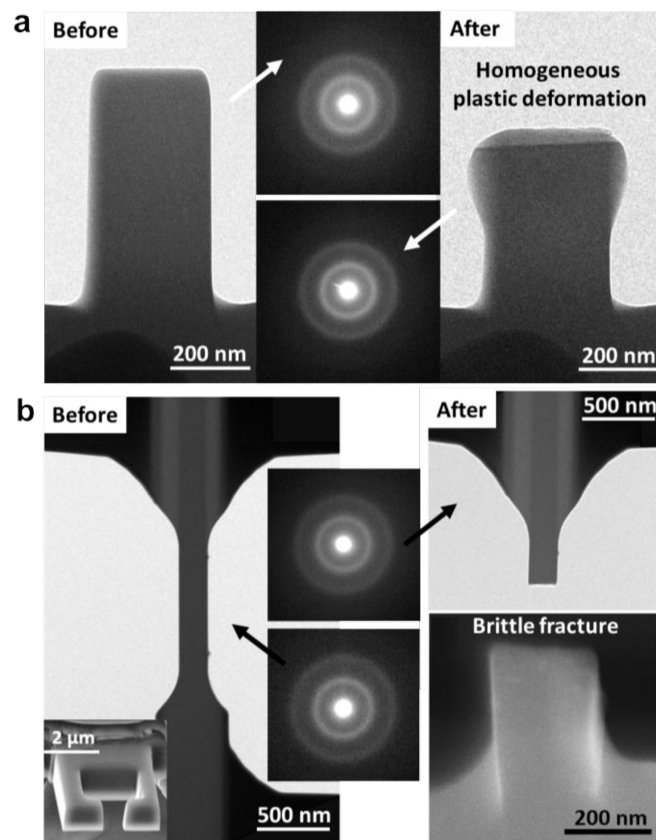


**Fig. SI-3** | (a) TEM characterization of the FIB-fabricated a-Si pillar before (left) and after (right) compression. The mushroom-like morphology of the deformed a-Si pillar

indicates homogeneous plastic flow without shear-off. The halos in the diffraction pattern of the pillar indicate that there is no crystallization throughout the compression.

**(b)** A prototypical “dog-bone” shaped tensile sample and its fracture surface. The flat fracture surface perpendicular to the tensile direction indicates that the fracture is brittle with little plastic deformation. The halos in the electron diffraction pattern of the fracture indicate that there is no crystallization.

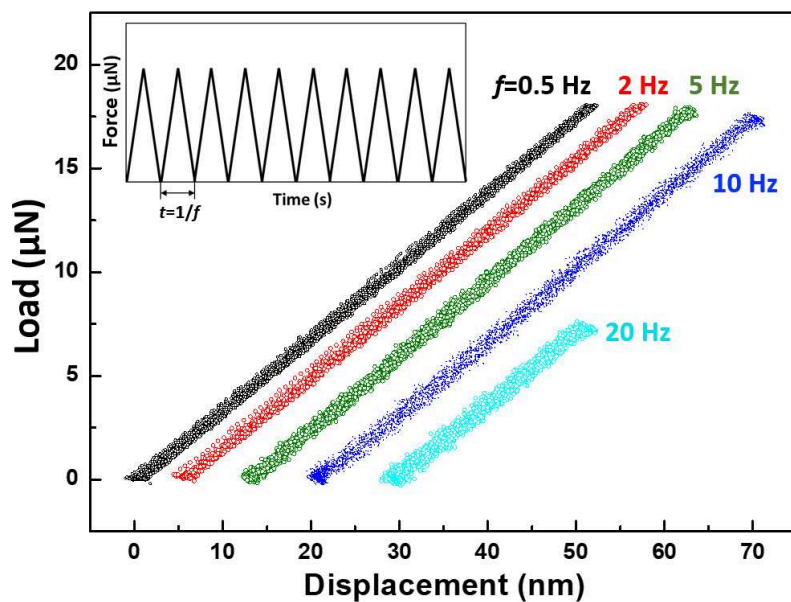


**Fig. SI-4** | Load-displacement curves obtained by cycling an empty PTP device (without any samples) 10 times using the nano dynamic mechanical analysis (nano-DMA) technique. The dynamic tests were subsequently conducted with load control using a  $\sim 7 \mu\text{m}$  flat-end diamond punch. To ensure the data reproducibility, 10 loading cycles were applied for each run of the dynamic tests. The inset spectrum of each load cycle was of a triangular shape, consisting of symmetrical loading and unloading portions. The perfectly overlapped loading and unloading curves at different frequencies (0.5 Hz, 2 Hz, 5 Hz, 10 Hz and 20 Hz) indicate that the PTP device itself shows perfectly linear elasticity behavior under this condition.

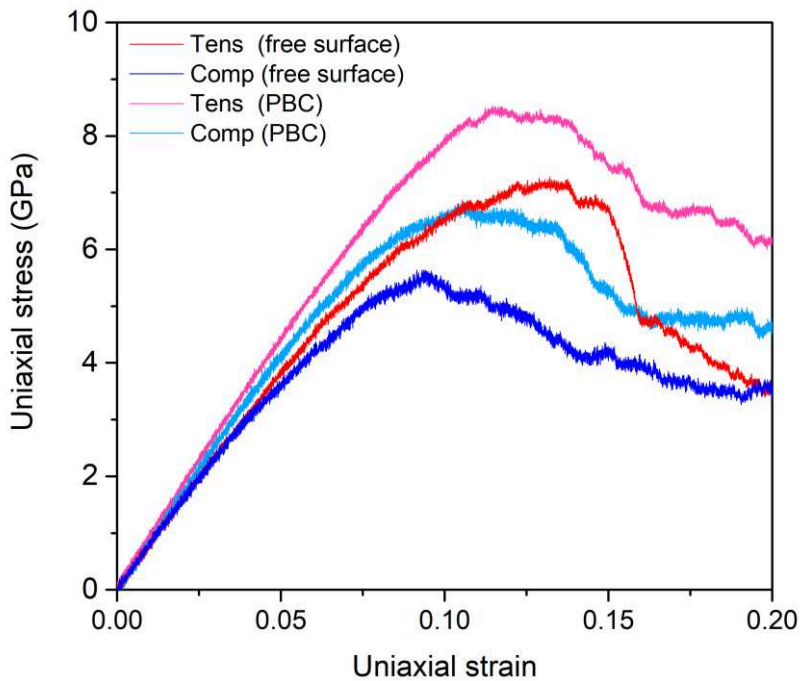


**Fig. SI-5** | MD-simulated stress-strain curves for uniaxial tension and compression along  $z$  axis at 300 K, for ML a-Si model with and without free surface in the  $x$  direction, while  $y$  and  $z$  directions are under periodic boundary conditions (PBC).

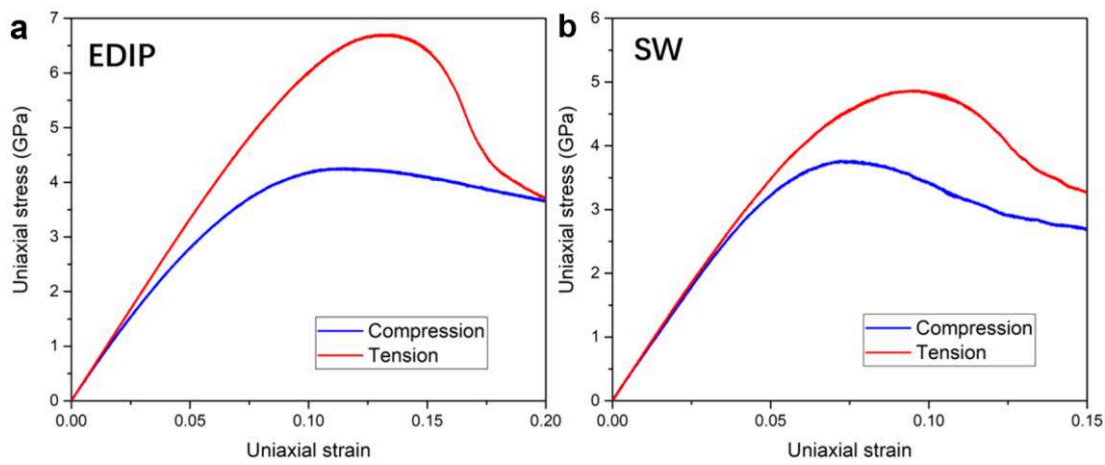


**Fig. SI-6** | MD-simulated stress-strain curves for uniaxial tension and compression along  $z$ -axis at 300 K for a-Si pillars (with a diameter of 20 nm), using (a) EDIP and (b) SW potentials.

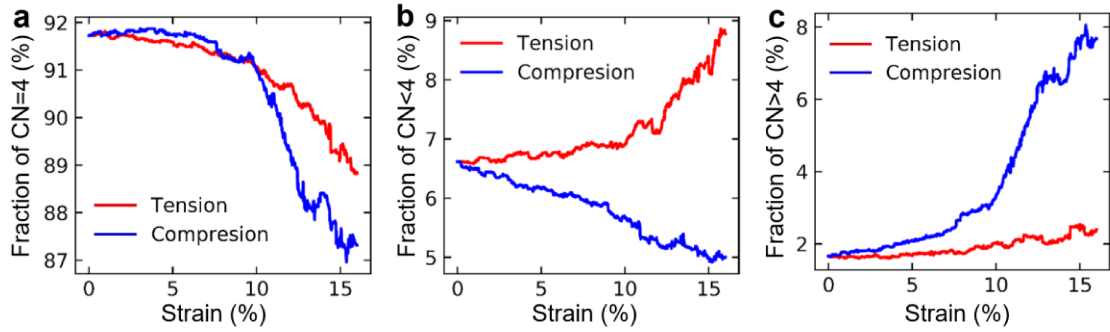


**Fig. SI-7** | Evolutions of CN with tensile and compressive strains. Dependence of the fraction of a-Si atoms with CN=4 (a), CN<4 (b) and CN>4 (c) on the tensile (red) and compressive (blue) strains, respectively. Note that some CN < 4 atoms are located close to the free surface.

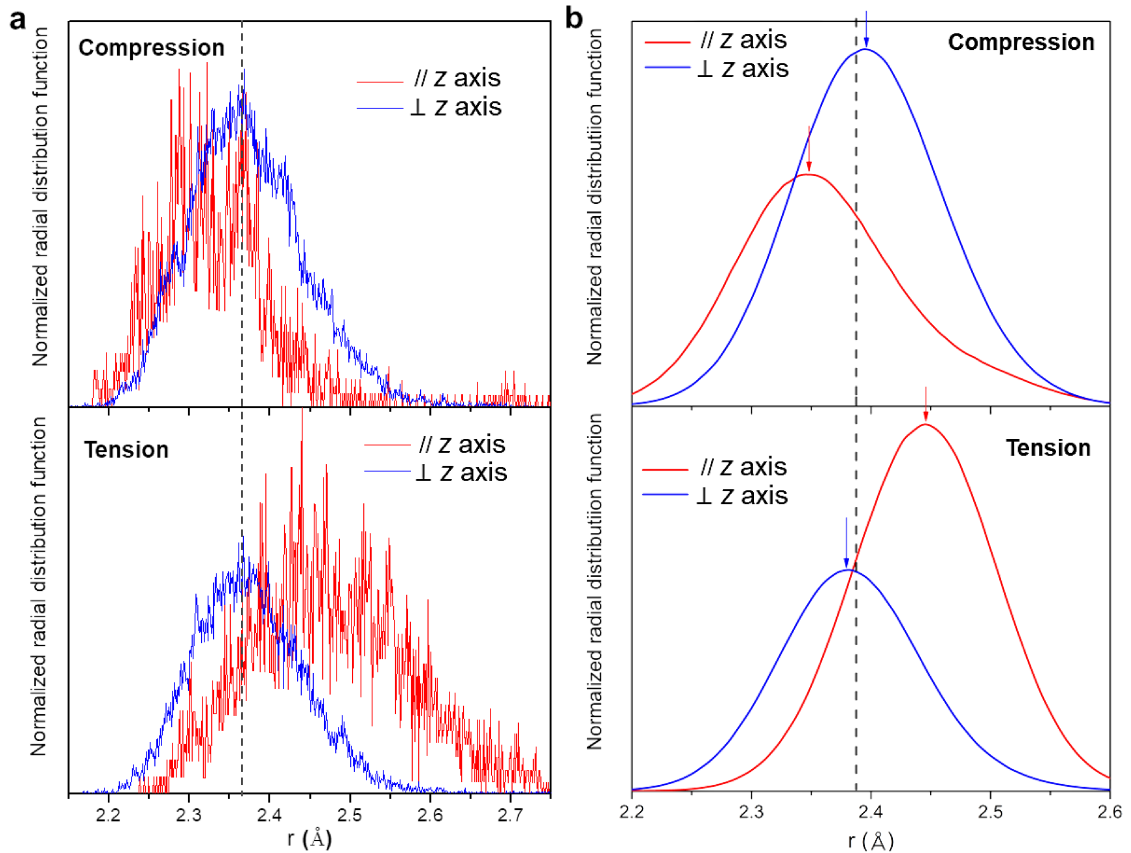


**Fig. SI-8** | Orientational radial distribution function (RDF) for the orientations parallel and perpendicular to  $z$  axis for the a-Si samples at the strain of 10% under compression & tension, simulated using ML potential (a) and EDIP potential (b). The dashed line indicates the first peak position of the undeformed a-Si sample. The orientational RDF  $g(r, \theta)$  is defined as  $g(r, \theta) = \frac{1}{\kappa \rho N} \sum_{i=1}^N \sum_{j=1}^N [\delta(r - r_{ij}) \cdot \delta(\theta - \theta_{z,r_{ij}})]$ ,

where  $\theta_{z,\mathbf{r}_{ij}} = \arccos(|\hat{\mathbf{r}}_{ij} \cdot \hat{\mathbf{z}}|)$  is the angle between the  $z$  axis and the vector  $\mathbf{r}_{ij}$ ,  $\mathbf{r}_{ij}$  is the vector connecting a central atom  $i$  to a neighboring atom  $j$ ,  $r_{ij} = |\mathbf{r}_{ij}|$ ,  $\rho$  is the number density,  $N$  is the total number of atoms in a sample,  $\kappa = 4\pi r^2 \Delta r [\cos(\theta - 0.5\Delta\theta) - \cos(\theta + 0.5\Delta\theta)]$ , and here we use  $\Delta\theta = 10^\circ$ . For clarity, we only contrast  $g(r, \theta)$  curves at two extreme ends, i.e.  $\theta = 5^\circ$  ( $\parallel z$  axis) and  $\theta = 85^\circ$  ( $\perp z$  axis), in these plots. The a-Si samples simulated using EDIP potential contain over 1 million atoms, about twenty times larger than those simulated using ML potential. The latter can only be applied for much smaller samples due to its extremely high computation cost; due to the small sample size and associated noise in the data, it is difficult to confirm the first peak shift for the orientation perpendicular to  $z$ -axis under compression versus tension (a). The bigger samples producing smooth curves (see b) are therefore useful: the peak shift now becomes readily observable (see the arrow pointing to the shifted peak).

### Supplementary Note 1:

In addition to the normal stress sign dependent shear moduli, we consider two previously known structural excursions in a-Si under stress/pressure. One is the polyamorphic phase transition, which transforms the low-density amorphous (LDA) state to the high-density amorphous (HDA) state, as demonstrated in previous studies<sup>1,2</sup>. But this polyamorphism requires an externally applied hydrostatic pressure as high as  $\sim$ 12-14 GPa in experiments and  $>10$  GPa in our MD simulation (Fig. SI-9). Such a magnitude is considerably higher than the compressive yield strength observed in our study. We can therefore rule out the LDA-HDA transformation as relevant to our T-C asymmetry. The other structural change is deformation-induced fertile sites for shear transformations, such as the increase of denser fivefold-coordinated liquid-like motifs converted from fourfold-coordinated solid-like ones<sup>3,4</sup>. However, this alone cannot explain the T-C asymmetry of a-Si, and especially the softening even at small strains. First, as clearly presented in Fig. 3d, the shear moduli have undergone noticeable

changes as early as in the nominally elastic regime, where the content of deformation-created liquid-like regions should be very low. Second,  $G_{xz}$  (or  $G_{yz}$ ) can even be increased rather than decreased upon straining when  $\sigma_n > 0$ . Third, the fraction of atoms with  $CN > 4$  remains rather limited throughout the deformation (Fig. SI-7). Therefore, the normal stress effect observed, especially in the early stage of deformation, cannot be accounted for solely by fertile sites created by shear transformations. Instead, two main factors are contributing to the T-C asymmetry. One is the above plasticity-induced fertile sites (softening), which becomes more important at large normal stress/strain (i.e., beyond elastic regime). The other factor is the anisotropic evolution of the shear moduli due to the imposed normal stress (see main text), starting from the early stage of deformation. With increasing  $\sigma_n > 0$  (tension), the modulus initially increases as the atomic arrangement evolves, but eventually decreases at large normal stress when activated shear transformations take over to convert many tetrahedral solid-like atomic environments into liquid-like fertile sites<sup>3,5,6</sup>. In comparison, at  $\sigma_n < 0$  (compression), both of these two factors contribute to softening, thus leading to decreasing shear moduli with strain in a fast and monotonic manner.

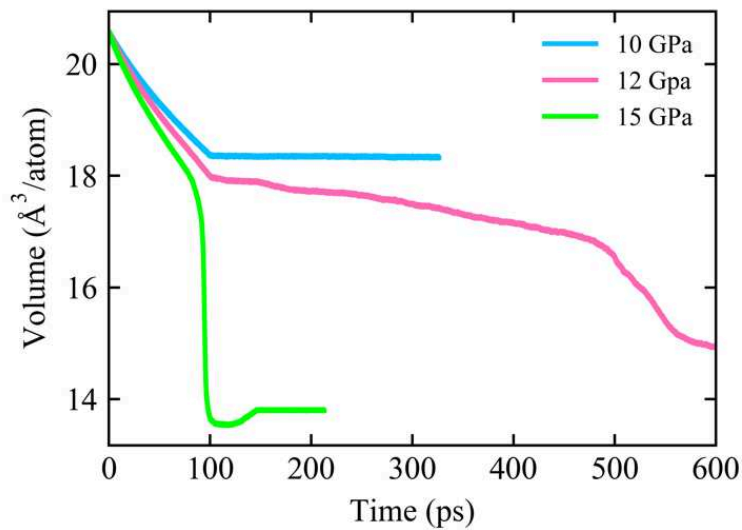


**Fig. SI-9** | The average atomic volume of ML modeled a-Si as a function of relaxation time under various hydrostatic pressure at 300 K. The hydrostatic pressure is increased at constant rate to target pressure during the first 100 ps and then kept constant.

In previous work, we have developed the flexibility volume parameter<sup>7,8</sup>,

combining mean squared displacement (MSD) and atomic volume, allowing universal prediction of  $G$  in metallic glass and a-Si at different compositions and cooling history. However, for the current case of a-Si under normal stress,  $G$  is no longer isotropic, and neither is the MSD. For example, as shown in Fig. SI-10a and 10b,  $MSD_z$  (MSD in  $z$  direction) is not equal to  $MSD_x$  or  $MSD_y$  ( $MSD_x=MSD_y$ ) under different normal stress in  $z$  direction. We therefore modify the previous definition to define an orientational flexibility volume parameter  $\lambda_{ij}$ ,

$$\lambda_{ij}=0.5\times(MSD_i+MSD_j)\times r\cdot\frac{(1+\varepsilon_k)}{(1+\varepsilon_j)} \quad (S1)$$

where  $i, j, k \in x, y$  or  $z$  directions,  $r$  is the average atomic spacing,  $\varepsilon_k$  and  $\varepsilon_j$  are the strain along  $k$  and  $j$ , respectively, after applying a normal stress. As demonstrated in Fig. SI-10c (also Fig. SI-11),  $G_{ij}$  of a-Si at different normal strains correlates very well with the inverse of  $\lambda_{ij}$ , suggesting that orientational flexibility volume is an effective structural parameter to characterize the mechanical property of amorphous materials.

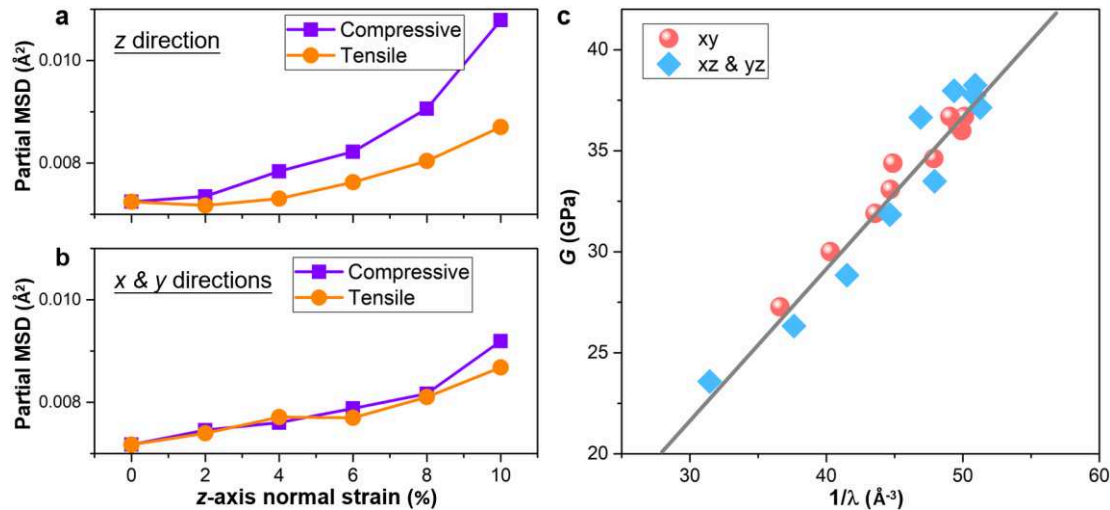


**Fig. SI-10 | Orientational flexibility volume parameter  $\lambda_{ij}$  unifying the anisotropic shear moduli at different normal stress.** The anisotropic MSD for (a)  $z$ -direction and (b)  $x$  or  $y$  directions when the ML a-Si model reaches different  $z$ -axis normal strains. (c) Correlation between the shear moduli  $G_{ij}$  and the inverse of the corresponding orientational flexibility volume. The straight line serves as a guide to the eye.

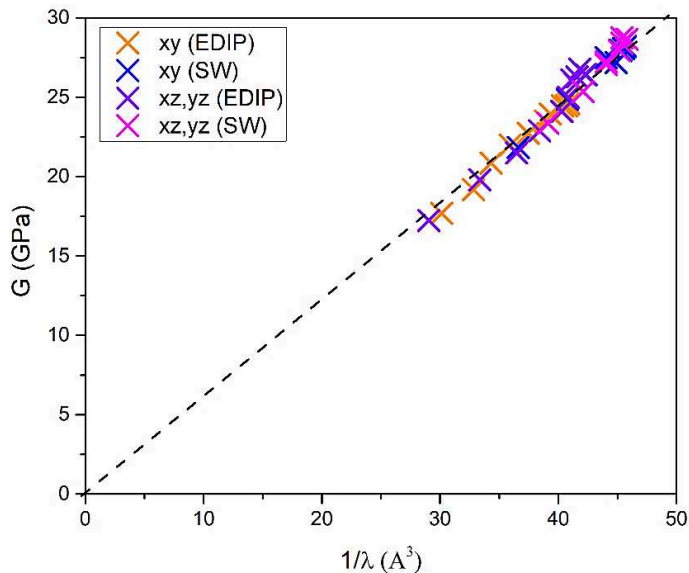


**Fig. SI-11** | A strong correlation is observed between the shear moduli  $G_{ij}$  and the inverse of the corresponding orientational flexibility volume, for MD-simulated a-Si using SW and EDIP potentials. The straight dash line serves as a guide to the eye.

## Supplementary Note 2: *In-situ* coupled mechanical-electrical tests for the resistance measurement

### Resistance measurement under tensile strain:

A-Si tensile sample was transferred to an electrical PTP (E-PTP) device, and both ends of the sample were welded on Au electrodes. More details about the E-PTP device can be found in reference<sup>9</sup>. The E-PTP devices matches with the Hysitron PI95 ECR TEM holder. The coupled mechanical-electrical test was performed inside TEM (JEOL 2100F, 200 kV). Firstly, the I-V curve was obtained by sweeping the voltage (V) from -0.1 V to 0.1 V and recording the electrical current (I) simultaneously. The linear I-V curve indicates the perfect Ohmic contact (Fig.SI-12a), and the resistance can be directly calculated with Ohm's law. Subsequently, a constant voltage of 100 mV was applied on the a-Si sample which is loaded via the diamond punch pushing the movable end of E-PTP, and meanwhile the current through the sample can be measured.

### Resistance measurement under compressive strain:

The Si wedge with a-Si pillar on its top was glued on a conductive copper sample mount using the conductive epoxy. The copper mount is screwed on one end of the ECR holder, and the other end of the holder is a conductive tungsten punch used for forming the circuit when touching the sample. In order to ensure the Ohmic contact (the linear relationship between voltage and current, Fig. SI-12b) and to avoid the localized deformation of a-Si induced by contact effect of the tip and pillar, the top of a-Si pillars was covered with a Pt cap during FIB fabrication. A constant voltage was applied upon the touch of W tip with pillar, and then the corresponding current was measured during compression.

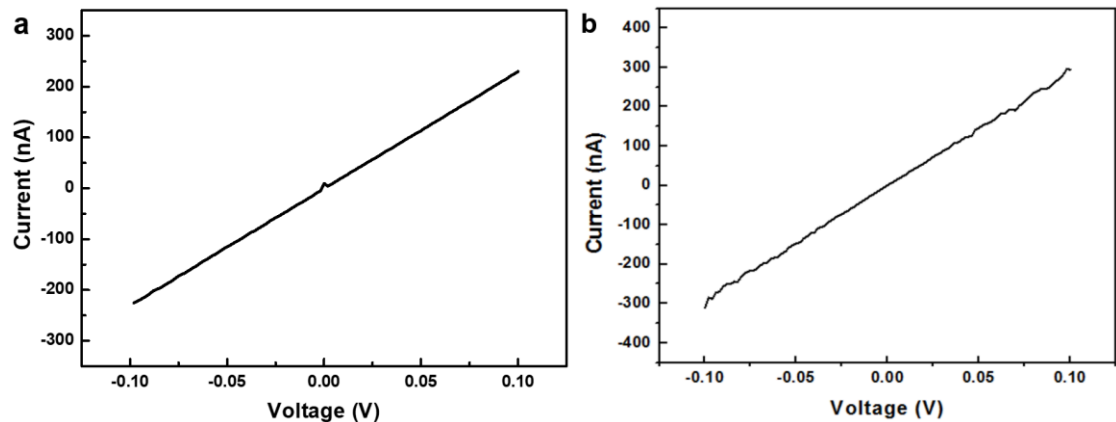


**Fig. SI-12** |  $I$ - $V$  curves were obtained by sweeping the voltage ( $V$ ) from -0.1 V to 0.1 V and recording the electrical current ( $I$ ), for mechanical-electrical coupling tests in tension (a) and compression (b). The linear  $I$ - $V$  curve indicates perfect Ohmic contact, and the resistance can therefore be calculated using Ohm's law.

### Calculation of resistance change caused by geometry change under straining:

The sample resistance ( $R$ ) is given by

$$R = \rho L / S \quad (\text{S2})$$

where  $\rho$  is the resistivity,  $L$  and  $S$  are the length and cross-sectional area of the sample, respectively. The sample volume  $V=S\times L$  is expected to be constant during the

homogeneous flow. At strain  $x$ , the length of a-Si under tension

$$L|_{(strain=x)} = L_0(1+x) \quad (S3)$$

where  $L_0$  is the initial length. As such, the resistance at strain  $x$  can be evaluated as

$$R|_{(strain=x)} = (\rho(L|_{(strain=x)})^2)/V = (L_0^2(1+x)^2)/V = R_0(1+x)^2 \quad (S4)$$

where  $R_0$  is the initial resistance.

Table S1 lists the a-Si samples information about their dimensions, initial resistances, the calculated and measured resistance changes under tension and compression, respectively.

**Table S1.** Sample dimensions and resistances change of a-Si under tension and compression

Sample	Diameter (nm)	Length (nm)	Initial Resistance (MΩ)	Resistance (Geometry change induced) (MΩ)	Resistance (at max strain) (MΩ)	Resistance (after unloading) (MΩ)
Tensile sample	188	3800	0.152	0.166	0.164	0.155
Pillar	200	310	0.342	0.248	0.186	0.253

The grey dashed line in Fig. 4a (in the main text) shows the resistance calculated using Eq. (S4) as a function of time (tensile strain). The curve agrees well with the measured resistance, indicating that the observed resistance increase during tensile deformation arises entirely from geometry change, and the resistivity stays constant.

This is no longer the case in the compression test, where resistance decreased from the initial 0.342 MΩ to 0.186 MΩ when the compressive strain reached -14.8% (see Fig. 4b in the main text). Upon unloading, the resistance of the pillar rose but only back to 0.253 MΩ after the sample was detached from the tungsten tip. The plastic strain of a-Si (measured from snapshots from the *in-situ* video) is about -5%, and the calculated resistance after unloading is 0.308 MΩ, higher than the measured resistance (0.253 MΩ). Given the resistivity of the deposited Pt cap is three orders of magnitude lower than that of the a-Si pillar<sup>10</sup> and that the size of the base beneath the pillar is very large,

the measured resistance should mainly come from the a-Si pillar. Besides, we also rule out the contribution from the elastic strain filed in the a-Si to the measured resistance change in our mechanical-electrical coupling experiment setup (Fig. SI-13).

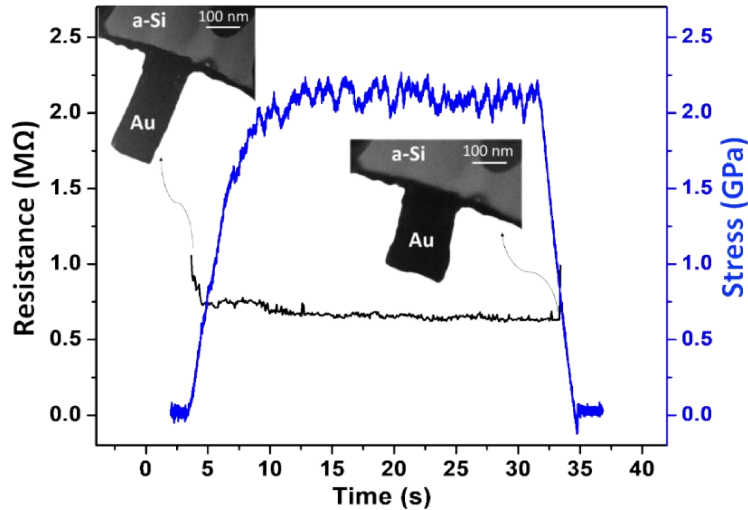


**Fig. SI-13** | Electrical resistance measurement of the a-Si base beneath the FIB-fabricated Au pillar. Soft Au film was deposited on a-Si, and then micromachined using FIB into pillar shape to form Ohmic contact with the tungsten tip. During the compression of the Au pillar, which has a low resistance that can be ignored compared with that of a-Si, the measured resistance stayed almost unchanged. This suggests that in our mechanical-electrical coupling experiment setup the elastic strain filed in the a-Si base has no contribution to the measured resistance change, which mainly comes from the geometry and resistivity of a-Si pillar under compression.

### Supplementary Note 3: the plasmon energy $E_p$ maps representing the (electron) density distributions of a-Si under tension and compression

In order to study the effect of tensile and compressive deformation on structure changes in a-Si, volume plasmon energy  $E_p$  maps were collected in a bent a-Si pillar on both its tensile side and compression zones<sup>11</sup>. As mentioned in the main text, the transformation from the tetrahedral solid-like (lower-density) state to the denser

fivefold liquid-like one is a crucial factor in the plastic deformation of a-Si. Therefore, it is important to measure the density difference between the tensioned and compressed a-Si for evaluating the structural change under tension and compression.

We performed electron energy loss spectroscopy (EELS) mapping on a bent a-Si pillar with a diameter of  $\sim 50$  nm (Fig. SI-14a) to obtain the density distributions in the tension and compression zones by measuring the volume plasmon energy  $E_p$ , which was successfully used previously to obtain the mass density of a-Si films<sup>12</sup>. Based on the free-electron assumption, the plasmon energy  $E_p$  is given by<sup>13</sup>:

$$E_p = \hbar \left( \frac{n_e e^2}{\varepsilon_0 m^*} \right)^{1/2} \quad (S5)$$

where  $n_e$  is the number density of valence electron,  $\hbar$  is the reduced Planck's constant,  $e$  is electron charge,  $m^*$  is the mass of electron, and  $\varepsilon_0$  is dielectric constant of the vacuum.  $E_p$ , which is proportional to the square root of the number density of valence electrons (also the number density of Si atoms if we assume the total number of electrons in the sample does not change), can be directly obtained from the EELS spectrum. The EELS data were acquired in a JEOL JEM-2100F STEM equipped with a Gatan Quantum 963 GIF. Standard imaging conditions have an accelerating voltage of 200 kV, a 40  $\mu\text{m}$  diameter condenser aperture, and an electron beam probe size of 0.2 nm. To determine the  $E_p$  of a-Si with high precision, we fit with Gaussians both the zero-loss peak and the first plasmon peak intensities in the EELS spectrum captured at each STEM raster. The two peaks are overlapped, the difference between the central energy of each peak is taken to be the energy loss  $E_p$  induced by plasmon oscillations. To determine the center energy of the zero loss peak and plasmon peak we used the method introduced in reference<sup>14</sup>. Each map contains 10×10 pixels on a 0.65 nm pitch. Repeated measurements at a single point give standard deviations in the  $E_p$  value of 15 meV~80 meV. As shown in Fig. SI-14, the compressively strained side shows much higher  $E_p$  and therefore larger valence electron density, compared with tension side. Furthermore,  $E_p$  mapping from the compression side shows larger heterogeneity with some local high  $E_p$  regions. According to Eq. (S5), we can get  $n_e / n_e' = (E_p / E_p')^2$ . The

maximum  $E_p$  measured in the compression side is 19.2 eV, and the average  $E_p$  measured from the tension side is 16.9 eV. The corresponding  $n_e$  has an increase of 25%. This increase is consistent with the conjecture that in local regions the coordination number increases from  $\sim 4$  (solid-like) to  $\sim 5$  (liquid-like), also a 25% increase.

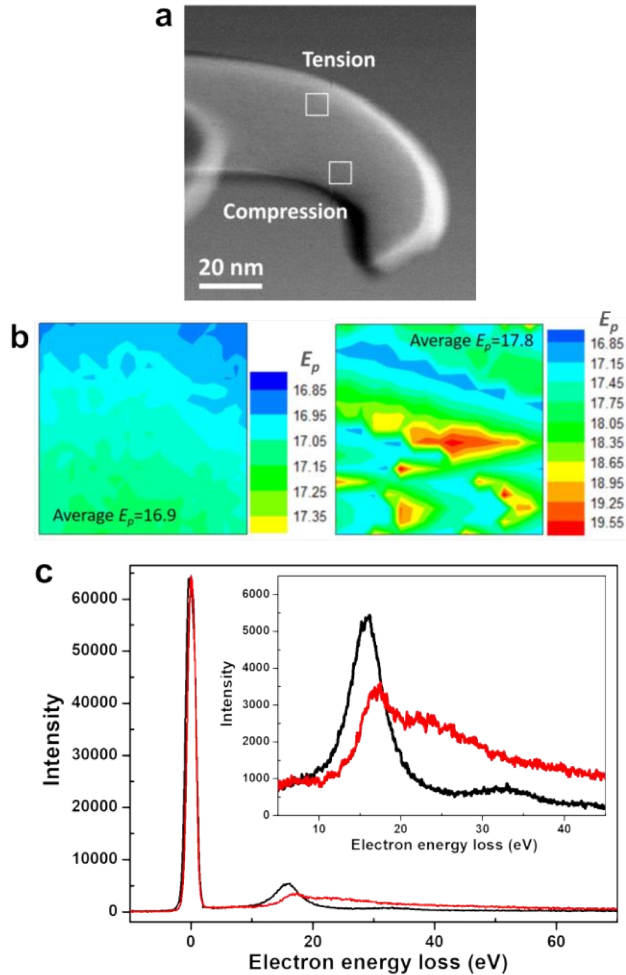


**Fig. SI-14** | Quantitative EELS was used to investigate the density difference between the compressive side and tensile side of a bent a-Si pillar with the original diameter  $d = \sim 50$  nm inside TEM. **(a)** STEM image of the bent a-Si pillar. **(b)** 2D contour image showing the plasmon energy  $E_p$  maps on the tension (left) and compression (right) zones marked by the white frames in (a). The compression side shows much higher  $E_p$  and therefore larger electron density, compared with the tension side. Furthermore,  $E_p$  mapping from the compression side shows larger heterogeneity with some local high  $E_p$  regions. This indicates that more liquid-like regions form as plasticity carriers under

compression, while the transformation from lower density to higher density is suppressed under tension. **(c)** The typical low-loss EELS spectra of  $E_p=17$  eV (black) and  $E_p=19$  eV (red) with the zero-loss peaks overlapped. The inset shows their enlarged plasmon peaks with different shapes and positions, and they correspond to the solid-like and liquid-like regions, respectively.

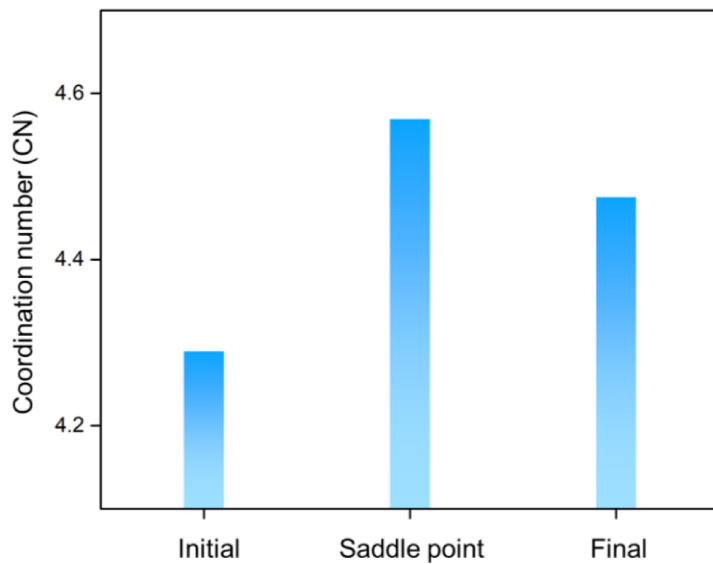


**Fig. SI-15 | Average coordination number for initial, saddle and final state of a-Si calculated using SW potential.** The search of saddle and final states of thermal activation events was performed using activation-relaxation technique (ART) package. Initial perturbations in ART were introduced by applying random displacement on a small group of atoms (an atom and its nearest-neighbors)<sup>15,16</sup>. The magnitude of the displacement was fixed, while the direction was randomly chosen. When the curvature of the potential energy landscape was found to overcome the chosen threshold, the system was pushed towards the saddle point using the Lanczos algorithm. The saddle point is considered to be found when the overall force of the total system is below 0.01 eV/Å. The corresponding coordination number of centered Si atoms was determined by the distance cutoff using the position of first minimum in pair distribution functions.

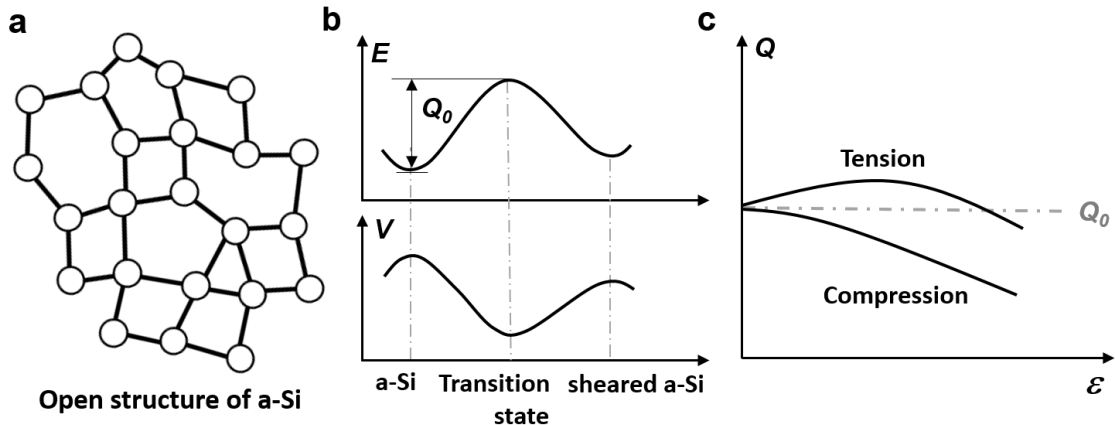


**Fig. SI-16 | Schematic illustrating the normal-stress-sign-dependent activation barrier  $Q$  for shear transformation events.** (a) Schematic showing the open network structure of the unstrained a-Si. (b) The energy  $E$ , as well as volume  $V$ <sup>17</sup> (also see Fig. SI-15 above), of a-Si in a shear deformation event, from the relatively low energy configuration to a metastable sheared configuration, crossing a transition state (saddle-point configuration) of higher energy and density. (c) Activation energy barrier  $Q$  as a function of strain  $\varepsilon$  under tension and compression, respectively, showing similar trends with the  $G$  change in Fig. 3d.

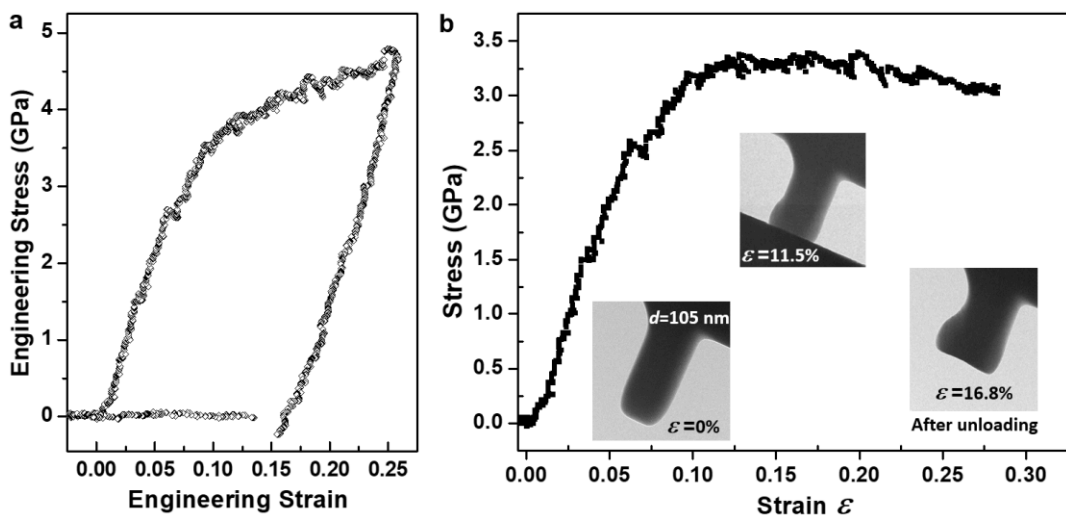


**Fig. SI-17 | (a)** Engineering stress-strain curve of an a-Si pillar with effective size  $d=105$  nm. **(b)** True stress-strain curve of the pillar. The true stress was calculated by dividing the deformed pillar's top area by the applied load. The insets show the morphology evolution of the a-Si pillar under compression.

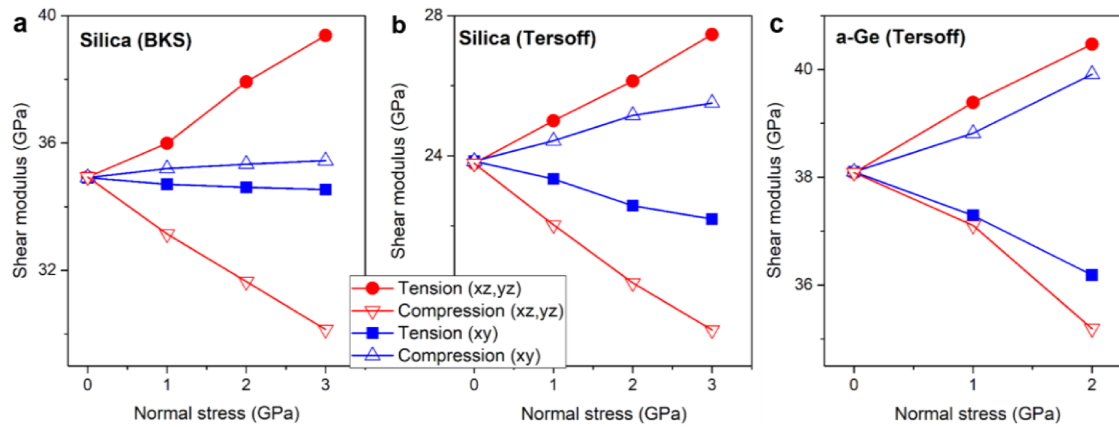


**Fig. SI-18** | Effects of normal stress ( $\sigma_n$  in  $z$  direction) on the shear moduli  $G_{xz}$  (or  $G_{yz}$ ) and  $G_{xy}$  of (a) silica using BKS potential<sup>18</sup>, (b) silica using Tersoff potential and (c) amorphous Ge using Tersoff potential.

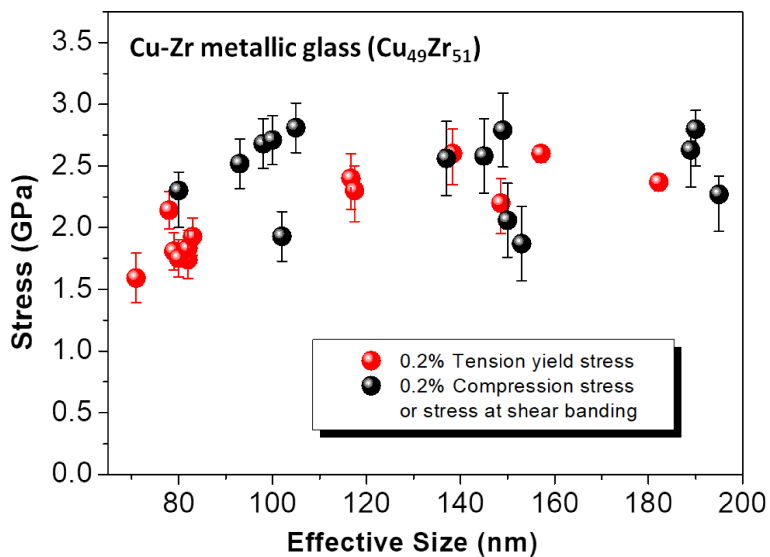


**Fig. SI-19** | Yield strength in tension versus compression, for submicron samples of a Cu-Zr metallic glass, showing only slight tension-compression asymmetry, with  $\sigma_c$  a little higher than  $\sigma_t$ .

## Supplementary References

1. Shimomura, O. *et al.* Pressure-induced semiconductor-metal transitions in amorphous Si and Ge. *Philos. Mag.* **29**, 547-558 (1974).
2. Daisenberger, D., *et al.* Polyamorphic amorphous silicon at high pressure: raman and spatially resolved

X-ray scattering and molecular dynamics studies. *J. Phys. Chem. B.* **115**, 14246-14255, (2011).

- 3. Demkowicz, M. J. & Argon, A. S. High-density liquidlike component facilitates plastic flow in a model amorphous silicon system. *Phys. Rev. Lett.* **93**, 025505 (2004).
- 4. Gerbig, Y. B., Michaels, C. A., Bradby, J. E., Haberl, B. & Cook, R. F. In situ spectroscopic study of the plastic deformation of amorphous silicon under nonhydrostatic conditions induced by indentation. *Phys. Rev. B* **92**, 214110 (2015).
- 5. Argon, A. S., & Demkowicz, M. J. What can plasticity of amorphous silicon tell us about plasticity of metallic glasses? *Metall. Mater. Trans. A* **39**, 1762-1778 (2008).
- 6. Demkowicz, M. J. & Argon, A. S. Liquidlike atomic environments act as plasticity carriers in amorphous silicon. *Phys. Rev. B* **72**, 245205 (2005).
- 7. Fan, Z., Ding, J., Li, Q. J., Ma, E. Correlating the properties of amorphous silicon with its flexibility volume. *Phys. Rev. B* **95** (2017).
- 8. Ding, J., Cheng, Y. Q., Sheng, H., Asta, M., Ritchie, R O, Ma, E. Universal structural parameter to quantitatively predict metallic glass properties. *Nature Commun.* **7**, 13733 (2016).
- 9. Wang, X. *et al.* Growth conditions control the elastic and electrical properties of ZnO nanowires. *Nano Lett.* **15**, 7886-7892 (2015).
- 10. Langford, R. M., Wang, T. X. & Ozkaya, D. Reducing the resistivity of electron and ion beam assisted deposited Pt. *Microelectron. Eng.* **84**, 784-788 (2007).
- 11. Wang, Y., Liang, B., Xu, S., Tian, L., Minor, A. M., Shan, Z. Tunable anelasticity in amorphous Si nanowires. *Nano Lett.* **20**, 449-455 (2020).
- 12. Haberl, B. *Structural characterization of amorphous silicon* Doctor of Philosophy thesis, The Australian National University, (2010).
- 13. Egerton, R. F. *Electron energy-loss spectroscopy in the electron microscope*. Springer Science & Business Media, (2011).
- 14. Mecklenburg, M. *et al.* Nanoscale temperature mapping in operating microelectronic devices. *Science* **347**, 629-632 (2015).
- 15. Barkema, G. T., Mousseau, N. Event-based relaxation of continuous disordered systems. *Phys. Rev. Lett.* **77**, 4358-4361 (1996).
- 16. Rodney, D., & Schuh, C. Distribution of thermally activated plastic events in a flowing glass. *Phys. Rev. Lett.* **102**, 235503 (2009).
- 17. Boioli, F., Albaret, T., Rodney, D. Shear transformation distribution and activation in glasses at the atomic scale. *Phys. Rev. E* **95**, 033005 (2017).
- 18. Kramer, G. J., Farragher, N. P., Van Beest, B. W. H., & Van Santen, R. A. Interatomic force fields for silicas, aluminophosphates, and zeolites: derivation based on ab initio calculations. *Phys. Rev. B* **43**, 5068 (1991).